CRANFIELD UNIVERSITY

SARA HAWI

A TESTBED FOR OPTIMAL COATING SELECTION FOR MICROMILLING OF BIOMEDICAL GRADE TI-6AL-4V

SCHOOL OF MANUFACTURING
MRes in Manufacturing

MRes
Academic Year: 2018-2019

Supervisors: Saurav Goel, Goncalo Rodrigues Pardal
July 2019

CRANFIELD UNIVERSITY

SCHOOL OF MANUFACTURING
MRes in Manufacturing

MRes

Academic Year: 2018-2019

SARA HAWI

A testbed for optimal coating selection for micromilling of biomedical grade Ti-6Al-4V

Supervisors: Saurav Goel, Goncalo Rodrigues Pardal
July 2019

This thesis is submitted in partial fulfilment of the requirements for the degree of MRes.

List of Publications

International Conference Proceedings

1. Hawi S., Dickins A., Pardal GR., Giusca C., Pearce O., Goel S., P 1.19- Fabrication of functionalised surfaces on Gum metal (Ti-30Nb) using micromachining, Proceedings of 19^{th} EUSPEN international Conference, Page 108-111, 2019, Bilbao, Spain

2. Hawi S., Goel S., Demystifying the composition and thickness of long-lasting commercially available tool coatings by the use of microscopy, MCM2019 Conference Proceedings, Page 401-403, 2019, Belgrade, Serbia

Poster Publications

1. Presented a technical poster on ”Demystifying the composition and thickness of long-lasting commercially available tool coatings by the use of microscopy” at the 14^{th} Multinational Congress on Microscopy held at Belgrade, Serbia, from 15-20^{th} September 2019.

2.Awarded Heidenhein scholarship award for the conference paper

3. Presented a technical poster on ”Fabrication of functionalised surfaces on Gum metal (Ti-30Nb) using micromachining” at EUSPEN 19^{th} international Conference held at Bilbao, Spain, from 3-7^{th} June 2019.

Abstract

One of the biggest challenges in precision micro-machining of titanium alloys is the tool wear as titanium is characterised as a “difficult to cut” material. Tool coatings provide a promising solution for the problem of tool wear while offering a low cost high value machining route.

This project aims to explore the design of engineering material systems along with machining parameters to guide the choice of tool coating while machining biomedical grade Ti-6Al-4V. The overarching aim is to identify a low cost tooling such as WC coated with the right coating composition together with the appropriate machining parameters. The research methodology applied to work towards this aim employs a design of experimental approach using the Taguchi method such that the spindle speed, feed rate and coating would be varied.

Both qualitative and quantitative analysis of the machining process was carried out to qualify the machining performance. During the machining trials, data was gathered and analysed to study the effect of cutting parameters on the specific cutting energy, material removal rate and surface roughness.

Acknowledgments

First and foremost, I would like to express my sincere gratitude to my supervisors especially Dr. Saurav Goel as he continuously supported, guided and motivated me throughout the duration of this project. I would also like to express my appreciation to Mr. John Hedge for assisting me in the micromilling experimental runs, Ms. Tracey Roberts for providing training on SEM-EDS equipment, Prof. Jose Luis Endrino from BCN (Basque, Spain) and Mr. Jose Santiago from PVT vacuum (Bensheim, Germany) for the support in DLC coating the microtools.

I am grateful to Cranfield University and the CDT in Ultraprecision for giving me the opportunity to study towards MRes in manufacturing, get an indepth view of the precision engineering field by attending industrial tours and participating in the EUSPEN 2019 conference.

Lastly, I would like to thank my colleagues, friends and family for the incessant emotional support they have provided me.

Contents

List of Abbreviations

WC	Tungsten carbide
DOE	Design of experiment
SCE	Specific cutting energy
MRR	Material removal rate
Ra	Average surface roughness or mean roughness value
f	Feed rate
SS	Spindle speed
PVD	Physical Vapour Deposition
CVD	Chemical Vapour deposition
HiPIMS	High power impulse magnetron sputtering
DLC	Diamond-like-carbon
OA	Orthogonal array
DOF	Degrees of freedom
EDS	Energy dispersive spectroscopy
SEM	Scanning electron microscope
OFAT	One factor at a time
fn	Function
HM	HardMax coating (TiAlN based)
UT	Union Tool coating (TiCN bases)

Chapter 1

Introduction

Titanium alloys have been widely used in various engineering sectors in particular aerospace, automotive and biomedical applications. Titanium alloys are of high interest to the manufacturing field due to them possessing high specific strength, exceptional corrosion resistance and fatigue resistance. However, they are classed as notoriously difficult-to-cut due to high rate of wear of the cutting tool, owing to high abrasion rate caused by thermophysical abrasive and adhesive mechanisms [1].

Ti-6Al-4V alloy is the most prevalent titanium alloy used in the manufacture of aerospace, automotive and biomedical components [2]. This is due to its high specific strength (177-206 kNm/kg), fatigue strength (529-566 MPa at 10^7 cycles), biocompatibility and corrosion resistance properties [3]. Extant research on machining of Ti alloys or Ti-6Al-4V is driven by the field of aerospace or biomedical engineering which seems to be the reason why most of the published work reports macroscale machining behaviour of these materials. However, the recent surge in the interest to obtain high accuracy, miniaturised components and functional micro/nano surface patterning has created a drive to improve the micromachining process of this alloy, a subject still in its outset, which is the motivation of this work.

1.1 Background

Micro/nano structured surfaces have motivated a push towards the functionalisation of surfaces in scientific, industrial, technological and engineering-wide applications [4]. For

instance, in tribological applications, surface texturing has been reported to enhance the performance of mechanical components both in research (e.g. magnetic hard discs, hydrodynamic bearings and articial joints) and in industrial applications (e.g. seals, pistons, and thrust pad bearing) [5]. In heat transfer management, nano structured/nano finned surfaces have been reported to enhance thermal energy conversion efficiency [6] [7]. This aspect is very promising for use in aircraft de-icing as ice formation on an aircraft's surface damages its aerodynamic shape and poses a threat to its safety [8]. A great potential of micro/nano structured surfaces applications has presented itself in the biomedical field as recent progresses in antibacterial surfaces suggest that surface micro/nano patterning can reduce the rate of bacterial infection of surfaces. This advancement has a very big impact on the quality of life as bone and joint degenerative and inflammatory problems affect millions of people around the world. According to Ribeiro *et al.* [9], these problems account for half of all chronic diseases in people over 50 years of age in developed countries. These degenerative and inflammatory problems such as osteoarthritis might be treatable with medication and exercise in the early stages but generally require implant surgery in more advanced stages. The introduction of an implant to the body is always associated with risks of bacterial infection. Figure 1.1 shows the possible routes of the implant post-surgery where it is either subjected to inflammation leading to failure or biomineralisation leading to osseointegration.

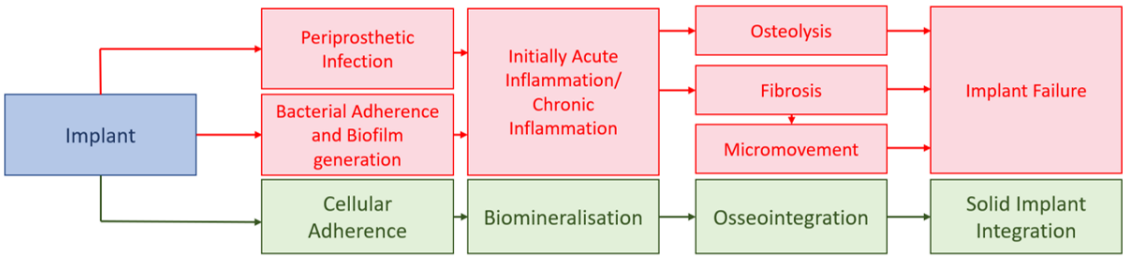

Figure 1.1: Different ways in which a medical implant may fail

The first most common route is linked to early infections that are often associated with bacterial contamination during surgical implantation. However, bacteria might remain on an implant surface, dormant, for several years before they trigger an infection [10]. The second most common route of infection occurs through haematological spreading from an

infection elsewhere in the body or periprosthetic infection. This route can unearth signs of infection any time after the surgery.

It has been researched that biomaterial-associated infections are the main cause of medical implant failure especially when dealing with high bacterial load in orthopaedic implants such as transcutanous pins [11] (Figure 1.2).

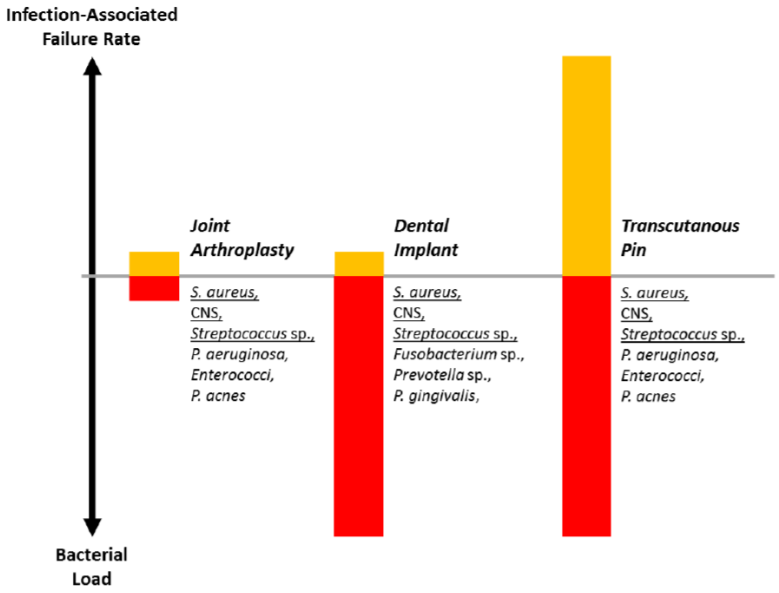

Figure 1.2: Infection-associated failure rate and corresponding bacterial load [11].

Implant failure often requires total implant removal, aggressive debridement and a prolonged course of antibiotics.

For these and many other application-oriented problems, surface micro/nano structuring is an emerging technological solution. Micromilling is one of the methods that allows the generation of these high accuracy three-dimensional micro-sized features/structures on a range of materials including biomaterials and aerospace materials with particular attention to Ti-6Al-4V, which is a widely used Titanium alloy in both fields. However, micromilling Titanium and its alloys is not an easy task as it is classified as a ”notoriously difficult to machine material” [12]. Therefore, there is a wide window of opportunity for new research to emerge towards improving the process of micromilling Ti-6Al-4V.

1.2 Aim and Objectives

The overarching aim of this project was to develop and elucidate an understanding of the micromilling process of Ti-6Al-4V by an improved process design which was assisted by the following few objectives set out to be delivered as part of this MRes research project.

- Conduct a thorough literature review on structured surfaces, end mill coatings and micromilling of Titanium alloys to formulate a new process design.
- Test and develop various microcoatings deposited on micro end mills and characterised by various kinds of microscopic techniques pre and post machining trials.
- Perform micromilling experiments incorporating Taguchi's design of experiment to gather output parameters (average surface roughness, material removal rate and specific cutting energy) as a function of input parameters (feed rate, spindle speed and coating).

1.3 Chapter Plan

Chapter 1 introduces the research background and the motivation behind the project. Research aim is presented along with the objectives that will build up towards achieving that aim.

Chapter 2 reviews the characteristics of Titanium and its alloys (Ti-6Al-4V) and the challenges encountered while machining them. It also presents the fundamentals and difficulties of contact mode micromilling as opposed to conventional milling. In addition, it reviews state-of-the-art in functional structured surfaces and tool coatings. Finally, it presents the theory behind Taguchi's design of experiment which was employed in this work.

Chapter 3 consists of the description of the experimental methods followed in this work. It first specifies the materials used, then the parameters used in DOE, the milling strategy employed and the hardware set-up for execution of experimental runs. In addition, it presents the methods and equipment used for post-process measurements.

Chapter 4 presents the results of pre and post-machining tool and tool coating material

characterisation. Details are provided for quantification of the specific cutting energy and material removal rate according to experimental data. Together with surface roughness data, it provides the rationale to link the output with the input parameters dictated by the DOE.

Chapter 5 draws the conclusions that are derived from the analysis presented in Chapter 4.

Chapter 6 presents recommendations and future work suggestions in order to build upon the knowledge gained in this work.

Chapter 2

Background

2.1 Titanium and its alloys

Titanium alloys are used in engineering sectors where weight, thermal stability, mechanical strength, hardness and biocompatibility are of primary concern [13][14]. Titanium's incomplete 3d orbital (e.g. [Ar]$3d^2 4s^2$ [15]) allows it to form solid solutions with many elements. The alloying elements of titanium alloys, subsequently the microstructure, dictates their properties which in turn dictate their applications.

Titanium alloys are split into four main types: α alloys, near α alloys, α - β alloys and β alloys [16]. The α phase has a hexagonal close packed structure while the β phase has a body centred cubic structure (figure 2.1).

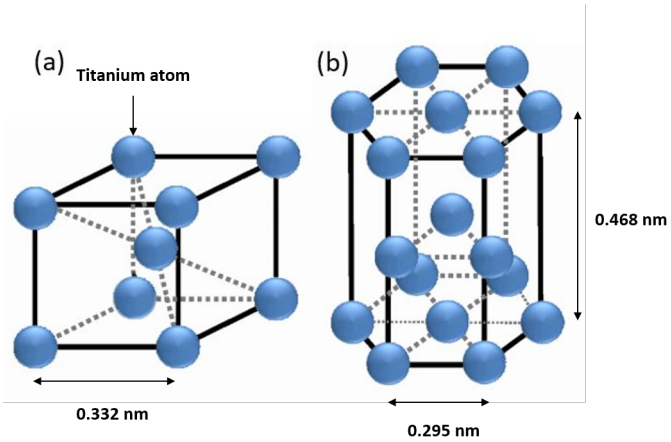

Figure 2.1: (a) Body Centred Cubic structure (β phase) (b)Hexagonal close packed structure (α phase) [17]

The α and near α alloys form in the presence of α stabilising elements such as aluminium, nitrogen, carbon and oxygen. As for the β titanium alloys, they form in the presence of β stabilising elements like vanadium, iron and manganese are present. Alloys like Ti-6Al-4V, containing both α and β stabilising elements are classified as α-β alloys. The main deformation mechanism for titanium alloys is dislocation slip. By comparison, β phase has a higher number of slip systems (e.g. 42 slip systems),whereas α phase has only three slip systems. However, in the β phase, as the planes are not close packed, the dislocations need higher shearing stress to move. Thus, α phase deforms more easily than β phase.

2.1.1 The Ti-6Al-4V alloy

This titanium alloy contains 6% Aluminium (α stabiliser) and 4% Vanadium (β stabiliser) which make it an α-β alloy. Its microstructure consists of primary equiaxed α grains and lamellar β phase as shown in figure 2.2.

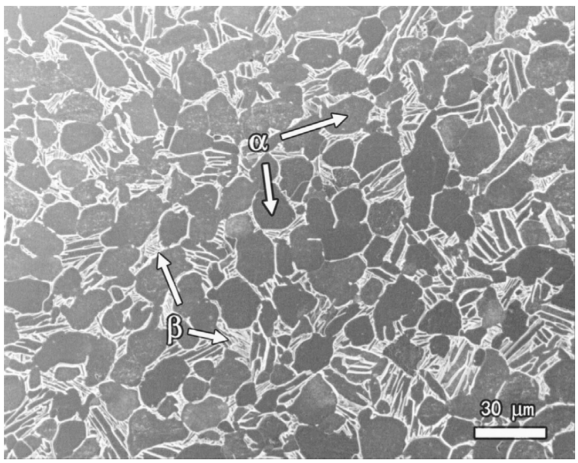

Figure 2.2: Bimodal microstructure of Ti-6Al4V [18]

At room temperature, the α phase is stable and the β phase is metastable.

2.2 Structured surfaces

Structured surfaces have gained a lot of attention due to a wide range of functionalities they possess. Natural surfaces have been at the heart of this rise in interest in structuring and texturing as they are the inspiration behind every functional surface developed. For instance, adhesion functionality was first observed through microscopic fibrils or pillars on the gecko's feet. Several researchers have replicated this fibril structure onto adhesive tapes using methods such e-beam lithography [19], photolithography along with chemical vapour deposition [20], replication through moulding using laser cut [21], etched, photolithographic or micromachined templates. Modified wetting behaviour was also observed on natural structured surfaces and most famously on the lotus leaf's hierarchical structured surface (figure 2.3). A range of studies have been conducted aiming at rendering surfaces hydrophobic (water repellent, water droplet/surface contact angle $\geq 90^o$) or superhydrophobic (water repellent, water droplet/surface contact angle $\geq 150^o$) [22]. Most recently, Huang *et al.*[23] have replicated the lotus leaf structure on polypropylene (PP) surfaces by injection moulding using nickel templates manufactured by electroless plating and electroplating from the natural lotus leaf original template. These surfaces exhibited a contact angle of around 157^o and roll off angle inferior to 5^o for a 4-μL droplet which makes them suitable for microdroplet transfer (i.e. micro-fluidics, lab-on-a-chip) and self-cleaning applications.

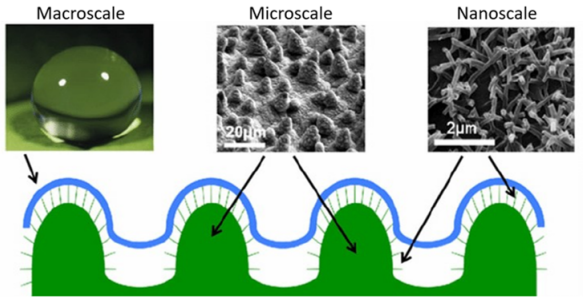

Figure 2.3: Micro/nano surface texture of the superhydrophobic lotus leaf. Reprinted with permission from [24], copyright 2011 Springer Nature.

Other structured surface functionalities such as anti-reflective (AR) properties were observed in the moth eye, cicada wing and butterfly wing. Various researchers have looked into AR structured surfaces for applications such as in photolithography for min-

imising replication errors [25], light emitting diodes (LEDs) [26], thermophotovoltaics (PVTs) [27], and solar cells [28] for enhancing their efficiencies. Burghoorn *et al.* [29] prepared moth eye-structured Ormocomp coatings on PMMA and PC, using a wafer-by-wafer step-and-flash Nano imprint lithography(NIL) process to achieve a reduction in reflection of 3.5% and 4% respectively.

Figure 2.4 presents a summary of methods utilised micro structuring of surfaces. Direct structuring methods can be used with all metals, ceramics, glasses and a wide range of polymers. Lithographic methods are generally used with metals, glass and polymers. As for alternative structuring methods; EDM is used to structure metals and conducting ceramics and etching methods can be used on metals and semiconductor materials, namely silicon.

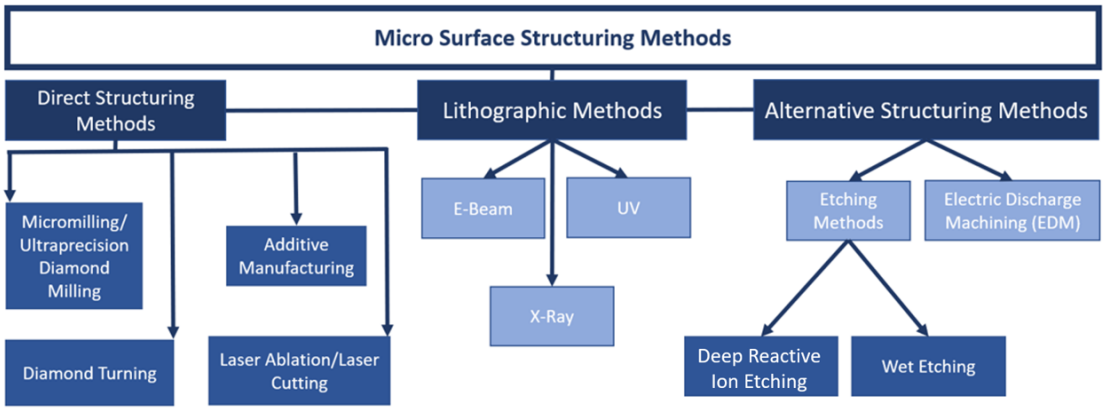

Figure 2.4: Micro surface structuring methods

Enhanced heat transfer has been shown to occur to structured surfaces (fins) as it increases the area exposed in convection. For micro-electro-mechanical systems (MEMs) and other miniaturised components that are subjected to heating during operation, micro/nanofins are critical in cooling and extending the life of these components. Wang *et al.* [30] introduced a textured copper asymmetric arc rib structure, on which arrays of secondary micro grooves were superimposed using an ultra-precision raster milling machine. Compared to conventional triangular rib structures, the arc rib microgrooved structures showed an improved heat transfer rate.

Functionalities such as bactericidal properties or antibiofouling properties have also been observed in nature and have attracted a lot of interest especially in biomedical appli-

cations.

2.2.1 Natural to man-made antibacterial surfaces

As presented in Chapter 1.1, in biomedical applications, the reduction of bacterial load on an implant, thus the reduction of bacterial adhesion is the point of interest. Therefore, a good starting point would be to understand the nature of adhesion mechanisms of bacteria to biomaterial surfaces.

Bacteria-Biomaterial Surface Adhesion Mechanisms

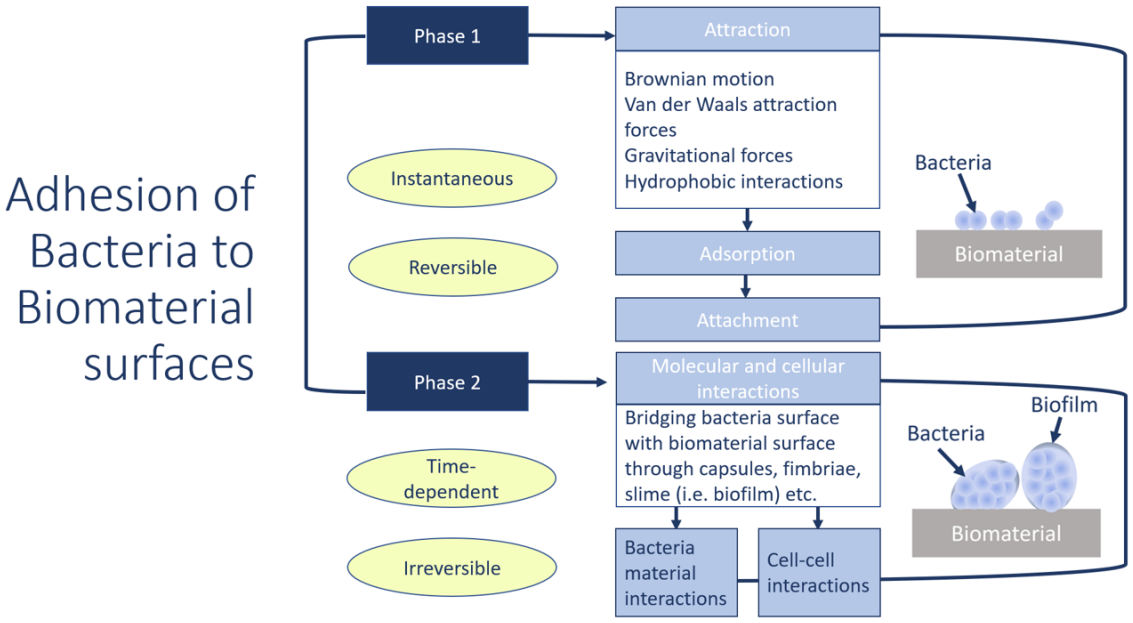

Figure 2.5: Adhesion mechanisms of bacteria to biomaterial surfaces

The adhesion of bacteria to biomaterial surfaces can be divided into two phases illustrated in figure 2.5. The first phase is instantaneous. It is governed by the attraction of the bacteria to the material through physiochemical interactions between both media such as Brownian motion, Van der Waals attraction forces, gravitational forces and hydrophobic interactions [9]. Those interactions determine the adsorption and attachment of bacteria to the biomaterial surface. This phase is reversible therefore it is the window of action for all efforts going towards reducing bacterial adhesion to biomaterials. Phase two is a time-dependent irreversible molecular and cellular phase. In this phase, two types of interactions occur and are dependent on each bacteria's bridging components such as

capsules, fimbriae, slime etc. The first interaction type is bacteria-material interactions and the second is cell to cell interactions where cells cluster and biofilm growth is prominent. Some bacteria do not produce slime thus do not compose biofilms which makes them easier to target through antibiotics, generally less adherent and less pathogenic [31].

The factors that influence bacteria adhesion to biomaterials are numerous but can generally be classified into three:

- Environment: Temperature, bacterial concentration etc.
- Bacteria Properties: Gram positive, gram negative, slime production etc.
- Material Surface Characteristics: Surface charge, hydrophobicity, surface roughness etc.

To counteract the first physiochemical bacteria adhesion phase (i.e. phase one) from an engineering perspective, an emphasis is put on material surface characteristics and more specifically on two surface functionalities, rendering surfaces antibacterial, inspired from nature: Anti-biofouling and Bactericidal properties.

2.2.1.1 Anti-biofouling Surfaces

'Anti-biofouling' is the inherent property of a surface to resist or limit the attachment of microbes/bacteria. This intrinsic property belongs to surfaces with unfavourable architecture or surface chemistry for attachment [32]. Marine organisms such as sharks, mussels, and crabs have natural anti-biofouling properties. For instance, The skin of the killer whale Orcinus orca has a system of ridges and grooves oriented transversely to the direction of flow [33]. In this case (like many others), the anti-biofouling property is not solely reliant on the topography but also on the surface chemistry whereas the skin possesses epidermal cells that secrete a mucosal coating that contributes to the antifouling properties of this marine animal.

Interestingly, the inner wall of a blood vessel or endothelium also possesses anti-biofouling properties which helps it to resist fouling from proteins and cells. Its topography is very distinct and is presented for the case of porcine pulmonary artery in figure 2.6 where a cobblestone-like morphology can be observed.

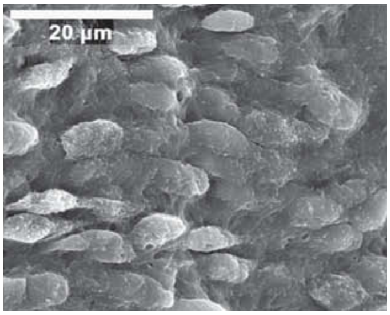

Figure 2.6: Porcine pulmonary artery's cobblestone-like morphology. Reprinted with permission from [34], copyright 2009 ELSEVIER

Again, the topography is coupled with chemistry to resist biofouling and in this case endothelial cells that contribute to repelling and inhibiting platelets, leukocytes, thrombosis and smooth muscle cell proliferation [33].

2.2.1.2 Bactericidal Surfaces

By definition, bactericidal surfaces are bacteria killing surfaces. Various insects and organisms resist or prevent bacterial adhesion by the use nanostructured/nanotexture surfaces to acclimate and survive in their environments [35]. For example, to maintain its superior aerodynamic performance, the dragonfly maintains the cleanliness and lightweightness of its wings by dust repelling, bacteria killing microscale and nanoscale surface topographies inducing both superhydrophobicity and bactericidal activity [36]. A micrograph of the dragonfly wing is presented in figure 2.7.

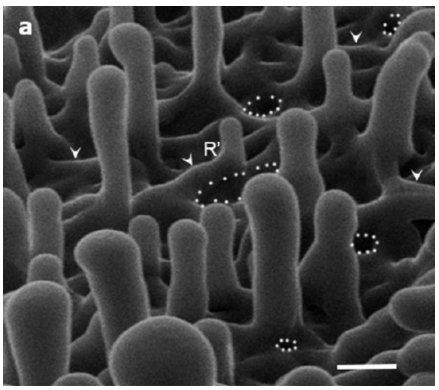

Figure 2.7: Helium ion micrograph showing the native nanopillars arrangement on the dragony wing. Reprinted with permission from [36] Copyright 2017 American Chemical Society.

A study conducted by Pogodin *et al.*[37] analysed the bacteria killing mechanism of

gram-negative bacteria by the cicada wing surface which comprises of nanostructures around 200 nm in height with a spacing and a tip radius of curvature of around 25-30 nm. It found that the killing mechanism is based on the adsorption of the bacteria to the nanopillars of the wing and the stretching of that bacteria which eventually leads to bacterial cell membrane rupturing. As opposed to previous models which theorised that nanopillars penetrate the bacteria membrane, this study proposed that the rupture of the bacteria wall occurs in the regions suspended between the nanopillars (see figure 2.8).

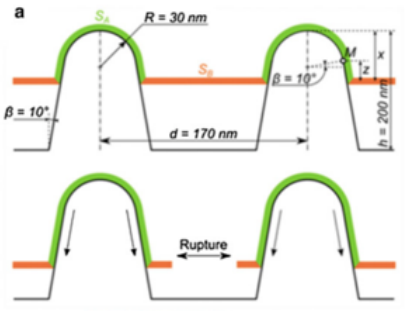

Figure 2.8: Biophysical representation of interaction between cicada wing nanopillars and adsorbed bacteria. Reprinted with permission from [37], copyright 2015 ELSEVIER.

A more generic quantitative thermodynamic model was developped by Li *et al.*[38] in which they studied the effects of nanopatterned surfaces (figure 2.9) on bacterial adhesion. They concluded that the physical origin of the bacterial adhesion to a nanopatterned surface is actually determined by the balance between adhesion energy and deformation energy of the cell membrane.

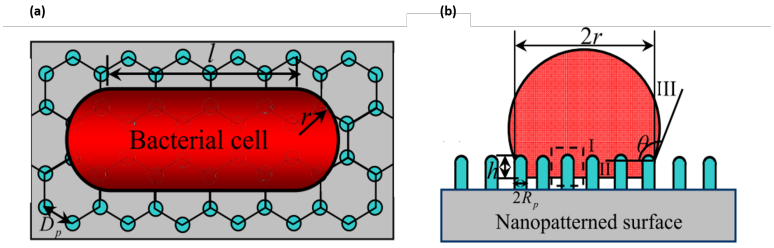

Figure 2.9: (a) Schematic illustration of a rodlike bacterial cell adhered to a nanopatterned surface with nanopillars. (b) The cross section along the radius direction of bacterial cell. Reprinted with permission from X. Li and T. Chen, "Enhancement and suppression effects of a nanopatterned surface on bacterial adhesion," vol. 052419, pp. 1–7, 2016. Copyright 2016 by the American Physical Society.

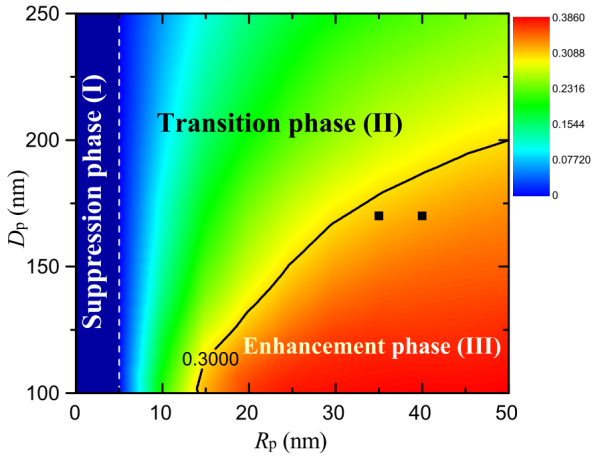

Figure 2.10: The phase diagram of the bactericidal activity in the space of R_p (nanopillar radius) and D_p (pitch between nanopillars). Reprinted with permission from X. Li and T. Chen, "Enhancement and suppression effects of a nanopatterned surface on bacterial adhesion," vol. 052419, pp. 1–7, 2016. Copyright 2016 by the American Physical Society.

The phase diagram shown in figure 2.10 was one of their findings, it expresses the relationship between R_p (the radius of the nanopillars' tip), D_p (the pitch between the nanopillars) and the enhancement or suppression of bacteria adhesion [38].

In biomedical and orthopedic applications, bactericidal behaviour is most wanted in orthopeadic materials, the most prevalent being titanium and its alloys. In addition, it is critical to be aware that the biocidal mechanism needed is a targeted one since the application requires in vivo interaction with eukaryotic cells. Attempts have been made in order to mimic the bactericidal behaviour of natural surfaces. Some of the most recent attempts are presented in table 2.1.

The majority of the surface structures developed have not been tested for in-vivo biocompatibility and for their ability to promote eukaryotic cells growth which hinders their advancement in orthopaedic implant applications.

Table 2.1: Nature inspired bactericidal surfaces

Surface Geometries	Material	Method	Biomimetic Basis	Bacteria targeted	Biocompatible	Reference
Nano needles/spikes 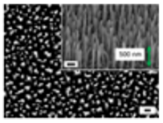	Black Silicon	RIE	-	Gram positive, Gram negative	no	[39]
Nano needles/spikes 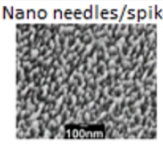	BDD coating on Black Silicon	RIE and CVD	Dragonfly Wing	Gram positive, Gram negative	yes	[40]
Nano needles/spikes 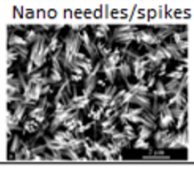	Titanium/TiO_2 nanospikes	Thermal Oxidation	Cicada wing	Gram negative	-	[41]
Nano-Spinules 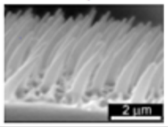	Biocompatible polymer	Nano-templating	Gecko Skin	Gram positive	-	[42]
Nanopillars 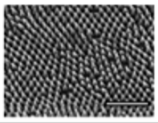	PMMA	nano imprint lithography (NIL)	Cicada wing	Gram negative	-	[43]
Nanocones 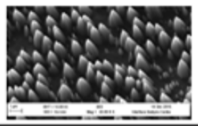	Silicon wafer/diamond nanocone	MPCVD and RIE	Cicada wing	Gram negative	-	[44]

2.3 Contact Mode Micromilling of Titanium and Its Alloys

Micromachining refers to the manufacturing of high accuracy three dimensional products whose features' sizes range from tens of micrometers to a few millimeters [45] [46]. In its traditional form, it includes microgrinding, microturning, micromilling and microdrilling. Table 2.2 presents the dimensional range of machining inputs and outputs for nano, micro and macromachining.

Micromilling technology is an extension of conventional milling that uses high precision cutting tools with predefined cutting edge geometries to remove material from the workpiece in order to fabricate complex three dimensional shapes and surfaces.

Table 2.2: Range of operations and achievable surface quality of nano, micro and macro-milling processes. Adapted with permission from [47] copyright 2012 Royal Society.

	Inputs				Output				
	Feed rate	Spindle speed	Depth of cut	Tool diameter*	Size of machined area	Volume removal in one machining step	Material removal rate	Relative figure error	Surface roughness (Sa)
Nano Machining	> 500 mm/min	> 50,000 rpm	≤ 100 µm	≤ 100 µm	$1\text{-}10^5$ µm^2	from 10^{-3} to 10^2 µm^3	from 10^{-5} to 1 µm^{3}s^{-1}	from 10^{-5} to 10^{-3}	$1\text{-}10^2$ Å
Micro Machining	< 500 mm/min	from 30,000 to 50,000 rpm	≤ 1 mm	from 100 to 500 µm	$1\text{-}10^5$ mm^2	from 10^{-3} to 10^2 mm^3	from 10^{-5} to 1 mm^{3}s^{-1}	from 10^{-7} to 10^{-5}	$1\text{-}10^2$ nm
Macro Machining	> 500 mm/min	< 30,000 rpm	≥ 1 mm	≥ 500 µm	$1\text{-}10^5$ cm^2	from 10^{-3} to 10^2 cm^3	from 10^{-5} to 1 cm^{3}s^{-1}	from 10^{-5} to 10^{-3}	from 10^{-1} to 10 µm

* For milling

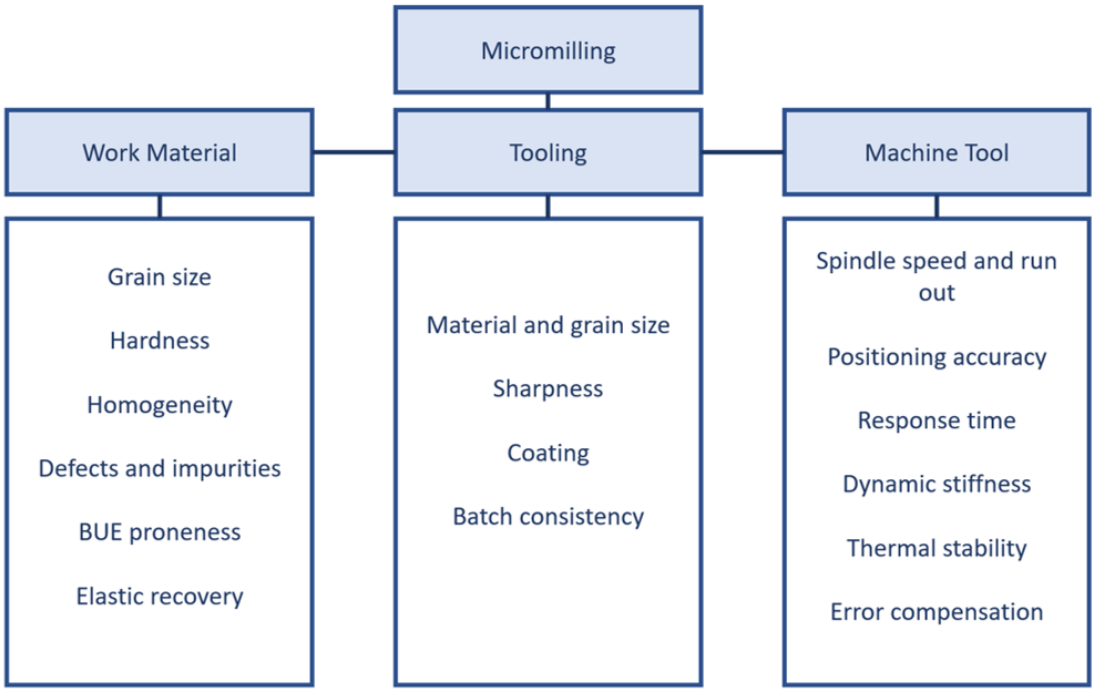

Figure 2.11: Key aspects influencing micromilling. Adapted from [48]

However, because of the scaling down of variables like depth of cut, cutting parameters and cutting tool diameters, the mechanism of micromilling is governed by different physical phenomena than conventional milling [49]. Key aspects that influence micromilling are shown in the figure 2.11.

For instance, the workpiece microstructure affects the process greatly as its grains are in the same order of the cutting tool diameter which results in a significant variation of product quality (surface roughness, burr formation, chip formation etc.) as workpiece microstructure varies (grain size, crystallographic orientation). The material of the tool along with its grain size are very critical in micromilling, they vary according to the workpiece

material characteristics and machining parameters used. The sharpness of the tool directly affects the surface roughness of the material, the coating affects the tool's longevity and wear rate and the batch consistency affects repeatability. Since micromilling tools are of small diameters, the machine tool is required to perform at high spindle speeds which hinders its dynamic stability. Therefore micromilling machine tools require better dynamic stiffness, motion/positioning accuracy and damping. Nonetheless, while running at high spindle speeds, thermal instability can cause dimensional changes through thermal expansion which lead to dimensional errors in the manufactured part. Thermal stability and thermal error compensation is an effective and cost-efficient method to reduce thermal errors [50].

Furthermore, when machining (micromilling) titanium and its alloys there is a very high temperature at the cutting edge of the tool. As the machining temperature increases, the heat stress increases since the heat dissipation of titanium through the cutting chips and the workpiece is low. This thermal stress emergence enhances diffusion and adhesion reactions between the tool and the workpiece as titanium possesses a high chemical reactivity at high temperatures [51].

Micromilling of titanium and its alloys has never been an easy task as they present low machinability due to their low thermal conductivity, high reactivity, low elastic modulus, high hardness and strength at elevated temperature, and peculiar work hardening features. Although titanium alloys are used in many engineering applications, there is limited published work on micromilling of these materials. Figures 2.12, 2.13 and 2.14 show various feed rates, spindle speeds and depths of cut versus tool diameters used in micromilling of titanium alloys gathered from literature [52].

In terms of feed rate values, there is a concentration on values below 200 mm/min. For spindle speed values, the parameters are generally more spread-out but most of the values are between 10000 rpm and 30000 rpm. As for the depth of cut values, there is a concentration between 10 and 30 μm.

Dickins [52] has utilised these concentrated values to find an optimised set of parameters for fabricating microgrooves on Ti-30Nb. He compared MRR outputs, burr heights and roughness values in order to conclude that low feed (50 mm/min), low spindle speed (20000 rpm) and intermediate cutting depth (10 μm) performed better in terms of burr

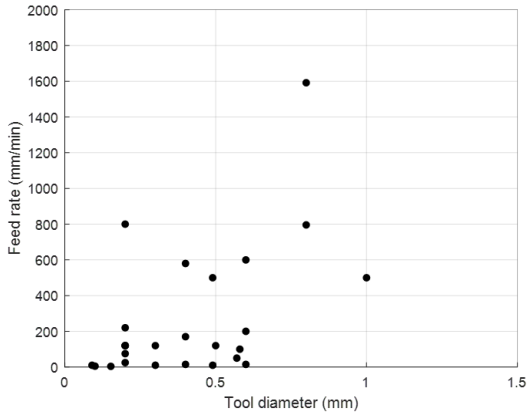

Figure 2.12: Various feed rate values vs. tool diameters used in micromilling titanium alloys. Adapted from [52].

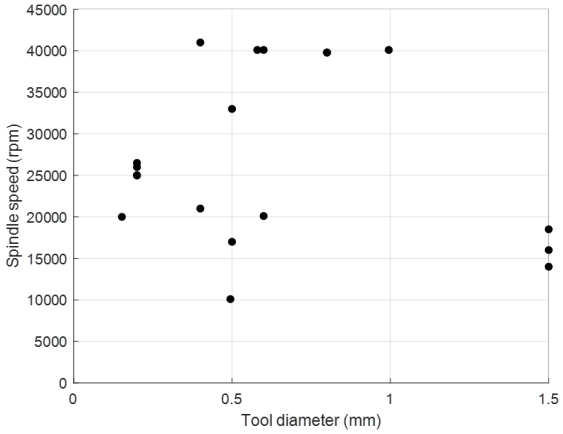

Figure 2.13: Various spindle speed values vs. tool diameters used in micromilling titanium alloys. Adapted from [52].

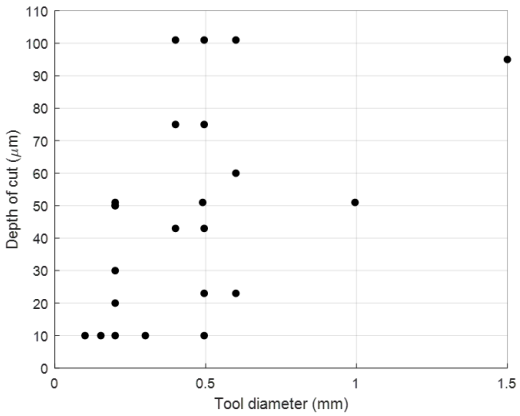

Figure 2.14: Various depth of cut values vs. tool diameters used in micromilling titanium alloys. Adapted from [52].

heights and roughness. Besides cutting parameters, cutting fluid has a large effect on the quality of the machined parts, both in terms of burrs formed and in terms of machined surface quality. Ziberov *et al.* [53] have confirmed this as they investigated the burr formation, tool wear, and surface finish while micromilling Ti-6Al-4V in both dry and MQL conditions. In addition, the tool life in dry machining was found to be longer; a fact which they attributed to BUE protection of the tool edge [54]. Furthermore, the choice of micromilling tool and coating affects surface quality and tool life greatly.

2.4 Micromilling Tools

2.4.1 Materials

Cemented tungsten carbide (WC) is a hard metal composite material that exhibits excellent wear resistance due to its unique properties combination of high density, high hardness, and moderate levels of fracture toughness. Cobalt is the most used metal binder for cemented carbides and especially tungsten carbide. At high temperatures, the solubility of WC in Co is high. In addition, Cobalt forms a liquid phase with WC which binds sintered parts together and produces a structures with low porosity. These properties make the use of W-C:Co tools widespread in machining applications.

2.4.2 Tool Wear

Tools used in mircomilling are of diameters less than 1 mm and operate at very high spindle speeds. They undergo high temperatures, changing chip thicknesses and recurring tensile and compressive stress. All of these conditions have a big impact on tool life. Furthermore, when working with hard to cut materials such as Titanium and its alloys, the tool life is cut even shorter by a high tool wear rate. The types of tool wear that could occur are illustrated in figure 2.15. Tool wear type is influenced by the machining regime. For example, in face milling, there is a cyclical change in thermomechanical stresses as the tool interchanges between cutting and idle strokes which causes cutting edge chipping

[55].

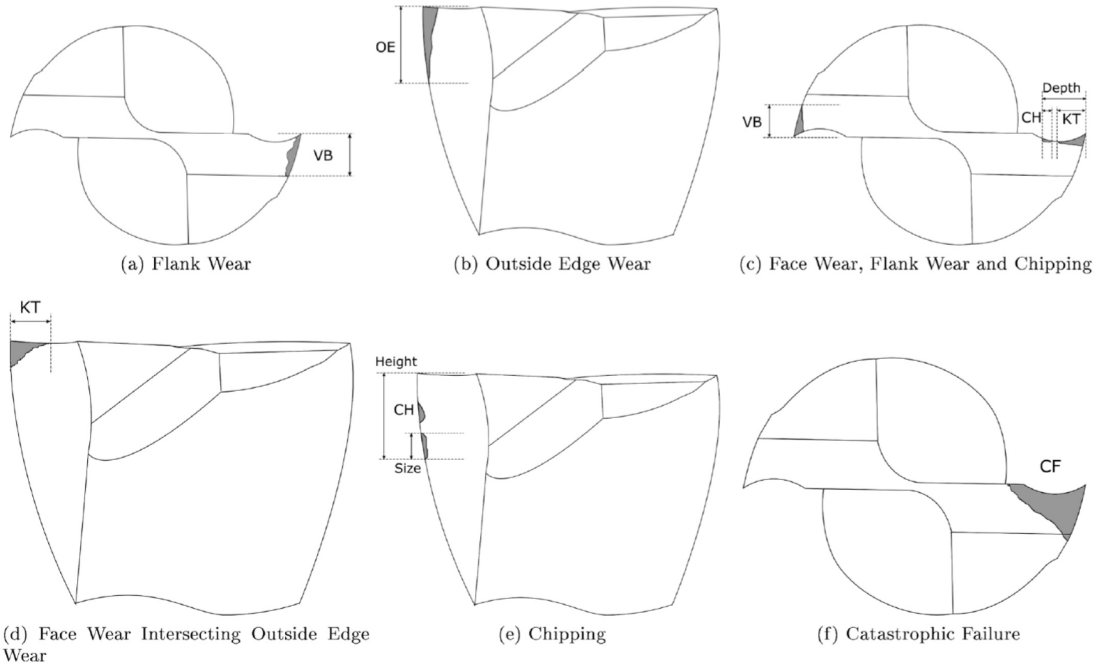

(a) Flank Wear (b) Outside Edge Wear (c) Face Wear, Flank Wear and Chipping

(d) Face Wear Intersecting Outside Edge Wear (e) Chipping (f) Catastrophic Failure

Figure 2.15: Types of tool wear [56]

In the aim of prolonging tool life and delaying the progression of wear, it has been proposed that thin wear resistant coatings be deposited on the tool.

2.4.3 Tool Coatings

The performance of the coating is strongly influenced by its mechanical and chemical properties, the cutting conditions and the workpiece material [57]. For milling applications, especially machining steels, TiN is a widely used coating. However, when it comes to machining hard to cut material such as titanium then TiN is not the recommended coating as it tends to form adhesion welding bridges at cutting temperatures above 300^o. In this case, elements such as Aluminium, Molybdenum, Chromium and Silicon are added to TiN providing an increased coating durability.

Functional multilayered tool coatings designed to target a range of complex problems encountered while milling have gained an increased research and industrial interest. Studies have been conducted towards the improvement of their properties by a directed selection

of mechanical and crystal-chemical characteristics of their individual layers and their sequencing [55]. In addition to the governing properties of each functional layer, multilayered coatings are more wear resistant than single layered coatings because each interface between the layers acts as a barrier to the crack propagation thus delays wear progression [58]. The architecture of multilayered coatings is presented in figure 2.16.

Multilayered coatings such as TiAlCrN/NbN have been observed to develop protective oxides under cutting conditions which allowed a prolonged tool life in contrast with TiAlCrN/Me_xN when milling hard AISI H13 (Me_x refers to transition metals Ta, Cr or W) [59]. Aramcharoen *et al.*[60] reported that AlCrTiN coated micro tools have reduced wear in comparison with uncoated tools when machining hardened die steels and that the effect of coating thickness does not reveal itself for short machining time but for long machining time, the thicker coating provides a better the performance.

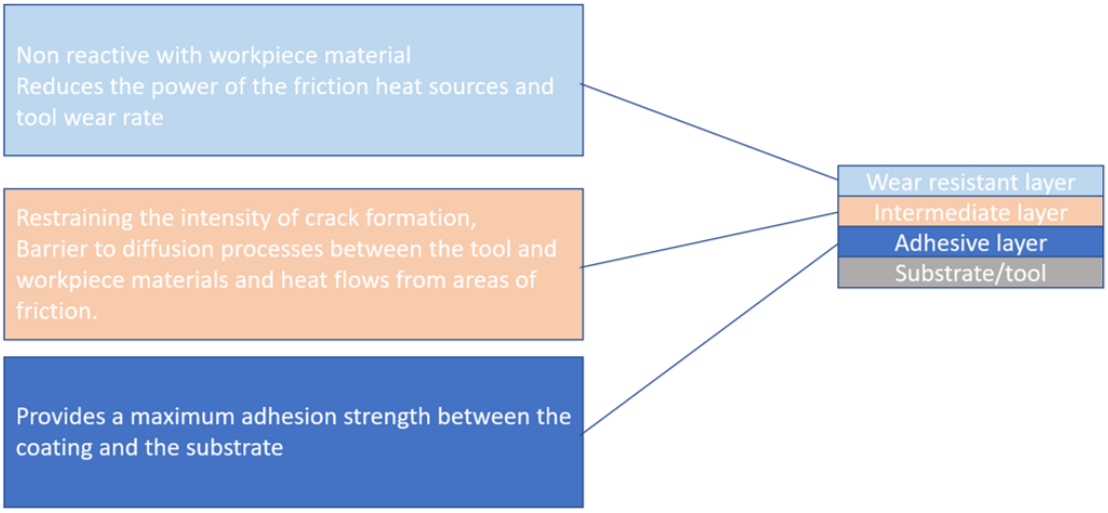

Figure 2.16: The layer sequencing of multilayered coatings

They have also studied the milling of hardened H13 tool steel with TiN, TiAlN, CrN and CrTiAlN coated tools and concluded that TiN performed best in terms of reducing two types of wear: edge radius wear and cutting edge chipping [61]. Darmawan *et al.* [62] have compared the progression of delamination wear of WC tooling coated with TiAlN/CrAlN, TiAlN/TiSiN, TiAl/TiBN and TiAlN for high speed cutting of abrasive particleboard. Their study concluded that TiAlN/CrAlN multilayered coating system per-

forms better than other coatings in terms of wear resistance and oxidation resistance.

Although the most common coatings are titanium based, some researchers have been investigating Diamond-like-carbon coatings due to their high hardness and low coefficient of friction against various materials. DLC consists of amorphous carbon (a-C) and hydrogenated alloys (a-C:H). The ternary phase diagram in figure 2.17 displays the compositions of the various forms of amorphous C-H alloys.

The high hardness of DLC and especially tetrahedral amorphous carbon (ta-C, Hardness

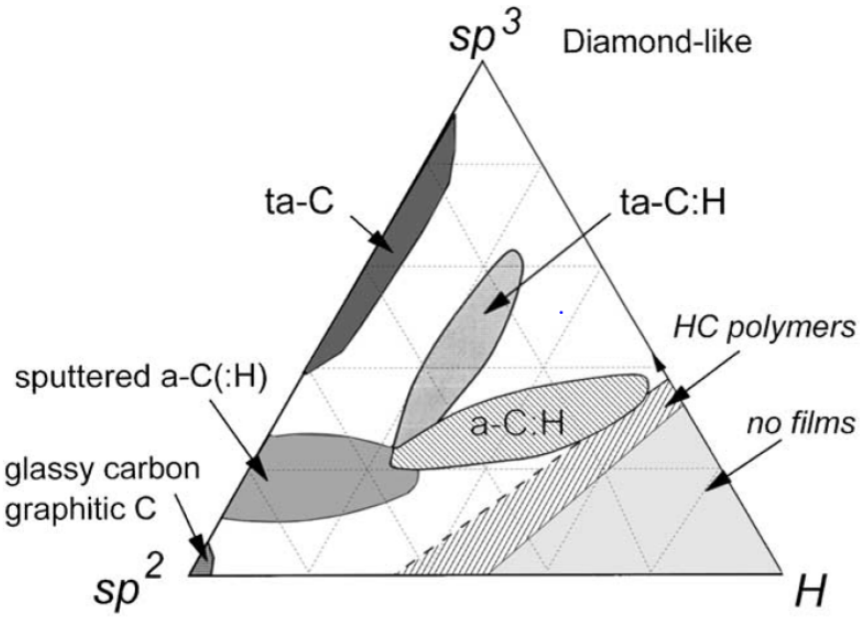

Figure 2.17: Ternary phase diagram of bonding in amorphous carbon-hydrogen alloys. Reprinted with permission from [63] copyright 2002 Elsevier.

$\approx$ 80 GPa) is attributed to the significant fraction of sp^3 bonds it contains. The superior properties of DLC enable them to lower the cutting forces and have higher wear resistance.

Metal doping or carbide doping DLC has been developed in the aim of improving DLC films' adhesion, thermal stability and toughness. These doped DLC films offer improved hardness and elastic modulus. For instance, tungsten Carbide doped (WC/C) hydrogenated DLCs prepared by PVD offer hardness values tailored by the coating process and can range from 500 to 2500 HV [64].

Figure 2.3 displays some of the commercially available DLC coatings and their properties (Deposited with HiPIMS technology). Wu *et al.*[66] deposited DLC films on tung-

Table 2.3: Commercially available DLC coatings (PVT Vacuum) and their properties [65].

Coating material	ta-C	a-C	a-C:H	Cr:DLC
Hardness (GPa)	35-40	15-25	25-30	30
Adhesion*	HF1	HF1	HF1	HF1
CoF (dry against steel)	0.1-0.15	0.08-0.14	0.05-0.10	0.08-0.12
R_a roughness (nm)	4-5	5	3-5	4-5
Max service temperature (°C)	500	400	350	***500***
Deposition rate (µm/h)	0.15	0.35	0.70	0.20
Deposition time (h)	13.5	6	4.5	10

*HF1 to HF4 adhesion acceptable, HF5-HF6 adhesion not acceptable
CoF: Coefficient of friction

sten carbide micro tools and concluded that the performance of DLC coated tools is superior to WC tools in dry cutting of Al6061 T6. Table 2.4 summarises the types of coatings mostly used on carbide microtools and their properties.

Table 2.4: Properties of coatings used on carbide microtools

Coating Type	Hardness (Vickers)	Max. Service Temperature (^{o}C)	Coating Color	References
TiN	2300	600	Golden-yellow	[66]
TiCN	3000	400	Blue grey	[67]
AlCrN-based	4000	>1100	Light grey	[66]
AlTiN-based	3600	1000	Grey	[66]
ta-C	3500-4000	500	Blue	[64]

2.4.4 Deposition Methods

Many coating processes are available, but only a few are among the most effective and applicable when dealing with micro-sized end mills. Those are mainly chemical vapour deposition (CVD) and physical vapour deposition (PVD).

Chemical vapour deposition is a deposition method that is based on the use of chemical precursors to form a thin film on a substrate by reacting in an isolated chamber [69]. CVD can be divided into several techniques depending on the method used to activate the chemical precursors. The most widely used methods are: Plasma enhanced chemical

vapour deposition (PECVD), plasma assisted chemical vapour deposition (PACVD) and thermal chemical vapour deposition. CVD techniques allow the deposition of thin films with high purity and density on complex geometries and shapes (substrate) with high deposition rates. For depositing DLC coatings and particularly a-C:H, PECVD is the most utilised CVD method [63]. Physical vapour deposition is a widely and industrially used coating method. The PVD process takes place in a high vacuum chamber where a solid material or target is vaporised (ionised or neutral), using either thermal evaporation or sputtering techniques, and then condensed on the substrate to be coated. The most common PVD coating processes are cathodic arc deposition, electron beam deposition, evaporative deposition, pulsed laser deposition, sputter deposition and High power impulse magnetron sputtering(HiPIMS). The latter being the newest emerging PVD technology. HiPIMS utilises extremely high-power densities of the order of 1-3 kW/cm^2 (compared to traditional magnetron sputtering 1–10 W/cm^2 [70]) in short pulses (impulses) of tens of microseconds (figure 4.5).

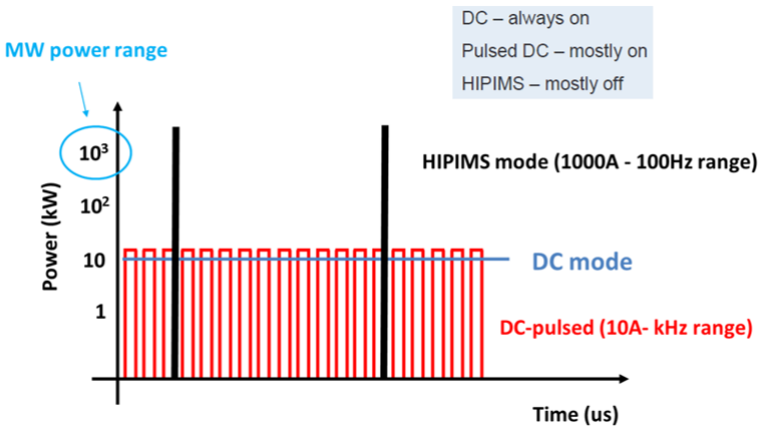

Figure 2.18: Difference in Power vs. time regime between DC magnetron sputtering, DC-pulsed magnetron sputtering and HiPIMS [65]

HiPIMS process delivers a large low-energy flux of ions to the substrate. This process takes advantage of enhanced ionisation, resulting from the high-energy pulse, thus which provides a high etching rate, high metal atom implantation on the substrate and enhanced adhesion of the thin film to the substrate. HiPIMS method has pushed the boundaries of PVD coatings to become considerably harder, tougher, denser, smoother

and more adhesive. Bobzin[65] suggested that for turning application, thicker CVD coatings are preferred due to their larger wear volume, whereas thinner PVD coatings are primarily recommended for milling applications due to the residual compressive stress and sharper cutting edges. Titanium nitride-based coatings are mostly deposited by magnetron sputtering, cathodic-arc and pulsed laser deposition techniques. On the other hand, Diamond-like-carbon (DLC) coatings are recently being deposited by the HiPIMS technique since it has improved their adhesion to the substrates especially when subjected to HiPIMS pre-treatment [71].

2.5 Taguchi's Design of Experiment

Design of experiment (DOE) is a robust technique of planning and designing an experiment with an aim that specific appropriate data is collected and analysed using statistical methods [72]. It is an efficient alternative to the traditional one-factor-at-a-time (OFAT) approach to conducting experiments which is time consuming, costly and sometimes unreliable as its results may not be repeatable or predictable.

Design of experiment based on the Taguchi methodology ensures that a systematic approach is followed in order to study the effects of various input parameters in an efficient and economical manner through a limited number of experiments. It requires less resources relative to the amount of information obtained as it varies several factors simultaneously. It helps in estimating the effects of each factor more precisely as it uses more observations to do so. In addition, factors' interaction can be estimated in a systematic manner as opposed to OFAT experiments where factors' interaction cannot be estimated [73].

Furthermore, process optimisation is more efficient using DOE as the experimental information are in a bigger region of the factor space which ameliorates the prediction of the response in the factor space [73] .

Taguchi divided optimisation into two categories; optimisation for a "static problem" and optimisation for a "dynamic problem".

A "static problem" (See figure 2.19 (a)) requires optimisation of a process which has several control factors that directly affect the desired output values. Thus it requires

the determination of the best control factors to meet the desired output. The aim of the optimisation is to minimise the variation of the output in presence of the noise in the process. When that is achieved, the process is said to have become ROBUST. A ”dynamic problem” (See figure 2.19 (b)) , involving an input signal that directly influences the output, requires determining the best control factors so that the input-output ratio is closest to the desired relationship. In this case, to minimise the variation of the output in the presence of noise, improved linearity in the input-output relationship is sought.

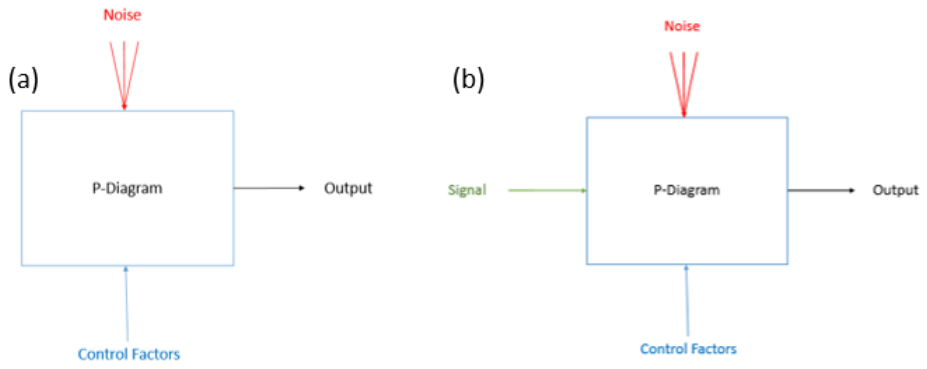

Figure 2.19: Process Diagram for a: (a) Static problem (b) Dynamic problem

For Taguchi’s DOE to be implemented, several steps have to be followed (refer to figure 2.20):

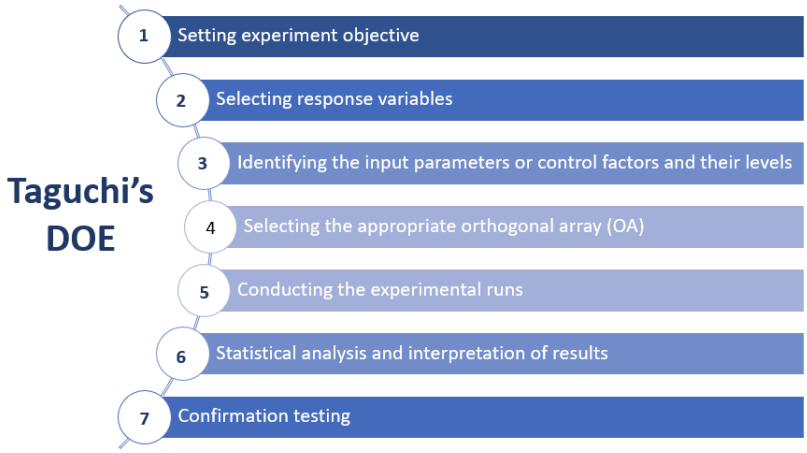

Figure 2.20: Taguchi’s Design of Experiment

- **Step 1: Setting experiment objective**

  Setting the objective of the experiment is a crucial first step into DOE and it paves the way into the next steps. It consists of determining the optimum performance that is sought and what it relates to (i.e. what parameter should be maximised/minimised).

- **Step 2: Selecting the response variables**

  A response variable denotes the output performance characteristic of the process undertaken. In DOE, it is widely favoured to choose quantitative response variables. In addition, the selected response should be affected, to a certain extent, by the input parameters or control factors.

- **Step 3: Identifying the input parameters or control factors and their levels**

  A list of input parameters or control factors stemming from deep research about what influences the ultimate objective should be put together. This step requires thorough review and research. Experience in the specific production process is often very helpful throughout this step.

- **Step 4: Selecting the appropriate orthogonal array (OA)**

  Orthogonal arrays are useful and essential tools for DOE. They possess the property that each factor level occurs the same number of times for every level of all other factors in the experiment. The ability to detect the presence of interactions between factors is the main reason that makes OAs essential for DOE. The selection of the most suitable orthogonal array for a specific experimental design is based on the the number of factors and interactions of interest and the number of levels for the factors of interest, all which determine the total degree of freedom calculated as [74]:

$$DOF = f(l-1) + i(f_i - 1)(l_i - 1) + 1 \tag{2.1}$$

  where f is the number of factors, l is the number of levels and i is the number of interactions. The degrees of freedom for the chosen OA should be greater than or equal to total degrees of freedom [75]. When this condition is met, the choice of OA

would depend on the combination of levels and factors used. Standard orthogonal arrays commonly employed are presented in table 2.5.

Table 2.5: Taguchi Designs Synoptic Table

Number of Variables	Number of Levels			
	2	3	4	5
2,3	L4	L9	L16	L25
4	L8	L9	L16	L25
5	L8	L18	L16	L25
6	L8	L18	L32	L25
7	L8	L18	L32	L50
8	L12	L18	L32	L50
9, 10	L12	L27	L32	L50
11	L12	L27	N./A.	L50
12	L16	L27	N./A.	L50
13	L16	L27	N./A.	N./A.
14, 15	L16	L36	N./A.	N./A.
From 16 to 23	L32	L36	N./A.	N./A.
From 24 to 31	L32	N./A.	N./A.	N./A.

- **Step 5: Conducting the experimental runs**

  The experimental runs should be conducted with some randomisation element. A randomised trial order protects the experimenter and the experimental results from accidental bias by randomising any unknown and uncontrollable factor that may vary during the experiment. The most used randomisation approaches are:

  1. Complete randomisation

  Complete randomisation means that any trial has an equal chance of being selected for the first test. The most basic application to simple randomisation is flipping a coin. For example, having two trials (trial number A and B), the side of the coin determines the assignment of the trials such that: heads assigns A as first trials and Tails assigns B as first trial.

  2. Complete randomisation within blocks

  This approach is used when one factor is very difficult or expensive to change the test set up for, but other factors' test set up can be changed relatively easily [76].

  3. Simple repetition

  In the simple repetition approach, any trial has an equal opportunity of being selected for the first test. However, after that trial is selected all the repetitions for that trial are tested.

- **Step 6: Statistical analysis and interpretation of experimental results**

To analyse the experimental results and measure the deviation of the outputs from the desired values, Taguchi suggested the use of signal to noise ratios (S/N). The term signal is used to denote the desirable value while the term noise denotes the undesirable value. The most used signal to noise ratios are divided into the following quality characteristics:

The-smaller-the-better:

$$S/N = -10log_{10}[\frac{1}{n}\sum_{n=1} y_i^2] \tag{2.2}$$

The-larger-the-better:

$$S/N = -10log_{10}\left[\frac{1}{n}\sum_{n=1} y_i^{-2}\right] \tag{2.3}$$

The-nominal-the-best:

$$S/N = -10log_{10}[\frac{\bar{y}^2}{s}] \tag{2.4}$$

where n the number of repetitions or trials, y is the performance measure, s is the sample variance and $\bar{y}$ is the mean of the performance measures.

The choice of the quality characteristic is dependent on the nature of parameter to be optimised[77]. For instance, when evaluating surface roughness the-smaller-the-better would be the suitable quality characteristic. After calculating the signal to noise ratios, a statistical technique called analysis of variance or ANOVA is used to determine which of the factors/interactions are significantly active. The total sum of squared deviations along with the degrees of freedom for each parameter can be calculated using:

$$SS_{parameter} = \frac{(\sum(S/N)_1)^2}{n_1} + \frac{(\sum(S/N)_2)^2}{n_2} + ... + \frac{(\sum(S/N)_a)^2}{n_a} - \frac{(\sum_{n=1}^{N} S/N)^2}{N} \tag{2.5}$$

and

$$df_{parameter} = a - 1 \tag{2.6}$$

Where (S/N) denotes the signal to noise ratio a denotes the number of levels of the

independent variable number of groups, N denotes the total number of observations in the experiment and n_1 denotes the number of observations in group 1 and so on.

The total sum of squares and the total degrees of freedom are calculated using [78]:

$$SS_{total} = \sum_{i=1}^{N} (S/N)_i^2 - \frac{(\sum_{i=1}^{N} S/N)_i^2}{N} \tag{2.7}$$

and

$$df_{total} = N - 1 \tag{2.8}$$

The following equations are the used to calculate the error and its degrees of freedom:

$$SS_{error} = SS_{total} - \sum SS_{parameter} \tag{2.9}$$

and

$$df_{error} = N - a \tag{2.10}$$

Finally, the contribution of each parameter can be computed using:

$$\%Contribution = \frac{F_{parameter}}{\sum F_{parameter} + 1} \times 100 \tag{2.11}$$

where F is the ratio of mean square of the specific parameter over the mean square of the error (often referred to as the Fischer test). However, since the mean square is equal to the sum of the square deviations over 2, then F can be computed as:

$$F_{parameter} = \frac{SS_{parameter}}{SS_{error}} \tag{2.12}$$

- **Step 7: Confirmation testing**

A confirmation test is used to verify that the estimated result agrees with the experimental result. If the optimal combination of parameters and their levels found coincidentally match with one of the experiments in the orthogonal array used, then the test is not required.

$$Y_{Optimum} = m + \sum_{l=1}^{L} (m_{lOpt} - m) \tag{2.13}$$

where m is the average of the output parameter that is to be optimised, L is the level, m_{lopt} is the optimum output parameter at the l level.

However, one must note that the results obtained in applying Taguchi's method are relative to the input parameters chosen and do not depict what parameter has the highest effect on the performance. In addition, since Taguchi's method makes use of orthogonal array and does not explore the whole range of combinations, it is not suitable for use whenever all interactions between parameters are needed. Not only that, but in the case of failure of one or more trials, the statistical analysis that follows would become invalid and adjustments of the levels and/or parameters has to be applied and the experimental work has to be repeated.

On the whole, functionalising titanium and its alloys through surface microstructuring is a challenging need for technological advancement which should be addressed in a systematic manner (DOE). A starting point would be to target one of the challenges that accompanies titanium micromachining; tool wear and premature failure. In the next chapter, the methodology followed in order to address this is detailed.

Chapter 3

Methodology

3.1 Materials

3.1.1 Workpiece Material

A 2200 mm x 32 mm x 20 mm Ti-6Al-4V bar was procured from TIMET (TIMETAL® 6-4 Titanium). It was then machined into smaller workpieces of 80 mm x 32 mm x 20 mm with four holes for fixturing as shown in figure 3.1.

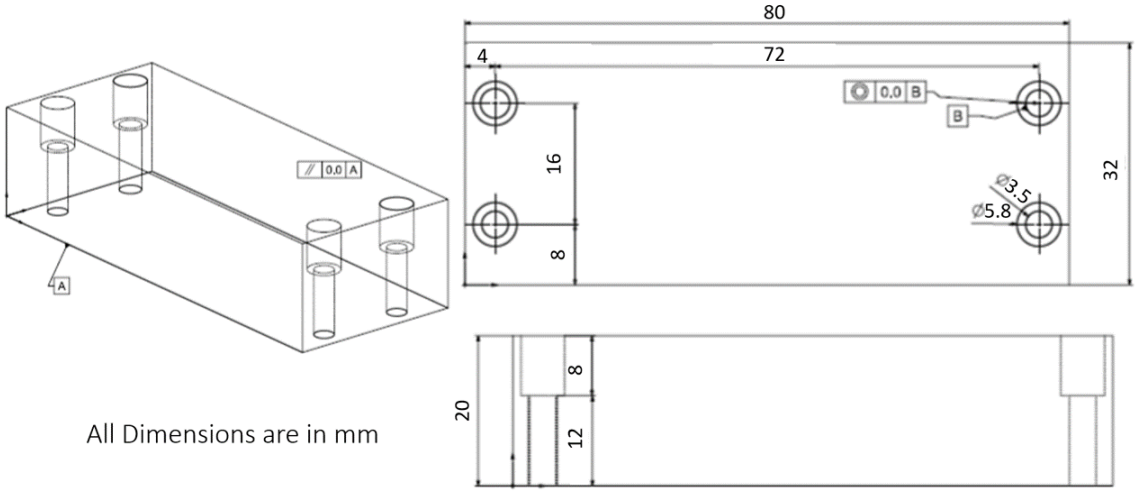

Figure 3.1: Ti-6Al-4V worpiece dimensions

3.1.2 Tools and Coatings

Uncoated Tungsten Carbide (WC) endmills were procured from Louis Bellet via Rainford Precision, the approved tool supplier for Kern EVO. Coated Tungsten Carbide endmills, with two types of coatings; a TiCN based coating and a TiAlN based coating were purchased from Union Tools via Rainford Precision. All tools were chosen with a nominal diameter of 200 μm. In-house High Power Impulse Magnetron Sputtering (HiPIMS) of DLC was attempted on uncoated WC tools using XPro4C (figure 3.2) in collaboration with PVT Vacuum. The coating structure is Cr/WC/ta-C with two variations in thicknesses; 300 nm and 400 nm. The tools were also inspected with the help of SEM (at Cranfield) and Raman spectroscopy (at PVT Vacuum).

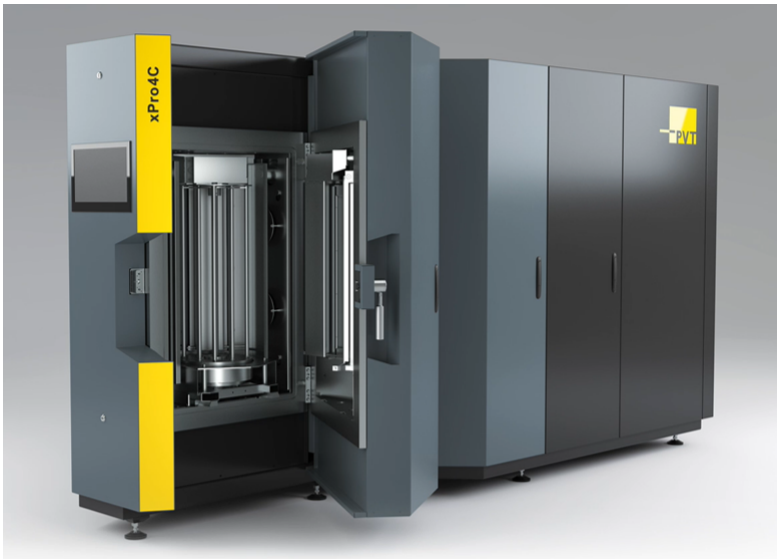

Figure 3.2: xProc4C coating system

Figure 3.3 shows one of the DLC coated tools. Its Raman spectroscopy results are presented in figure 3.4. For DLC films, there is dominant Raman light scattering only on sp^2 sites. In order to quanlitatively evaluate the DLC structure through Raman spectroscopy, the raman spectra is usually deconvoluted into two gaussians; a G-peak (Graphite) and a D-peak (Disordered) [79]. The DLC coated on the tool is Ta-c with very high sp^3 bonds. In the figure , a broad Raman peak can be seen around 1500 cm^{-1}. Graphitic (sp^2) clusters provoke the D peak in the raman spectra which is shown to be almost absent in the DLC coating raman spectra presented. The adhesion of the coating was classified as HF1 by PVT Vacuum according to the Daimler Benz Rockwell-C adhesion test which is

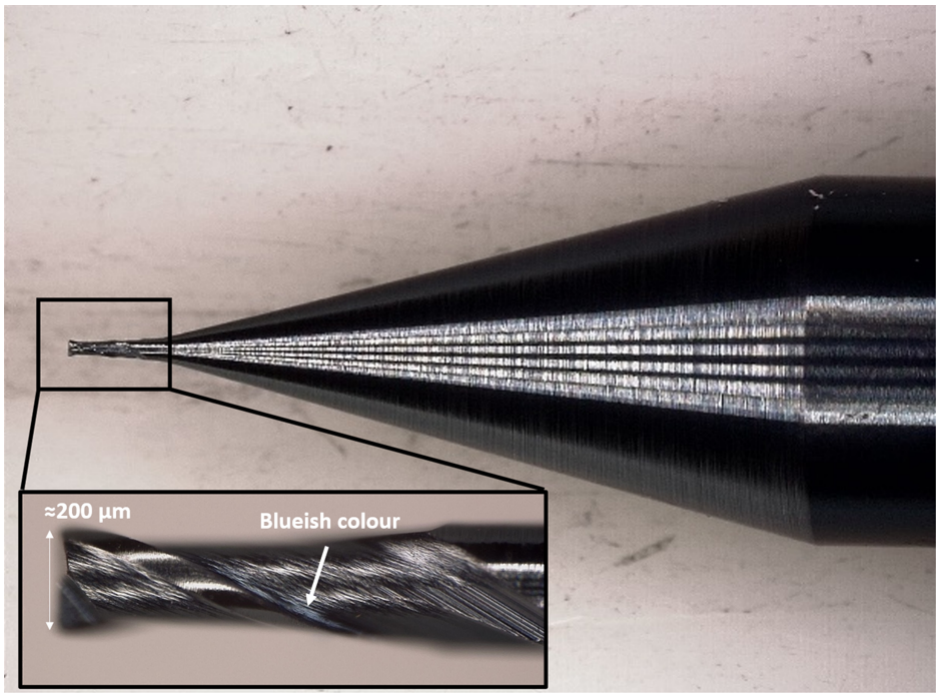

Figure 3.3: In-house DLC coated tool

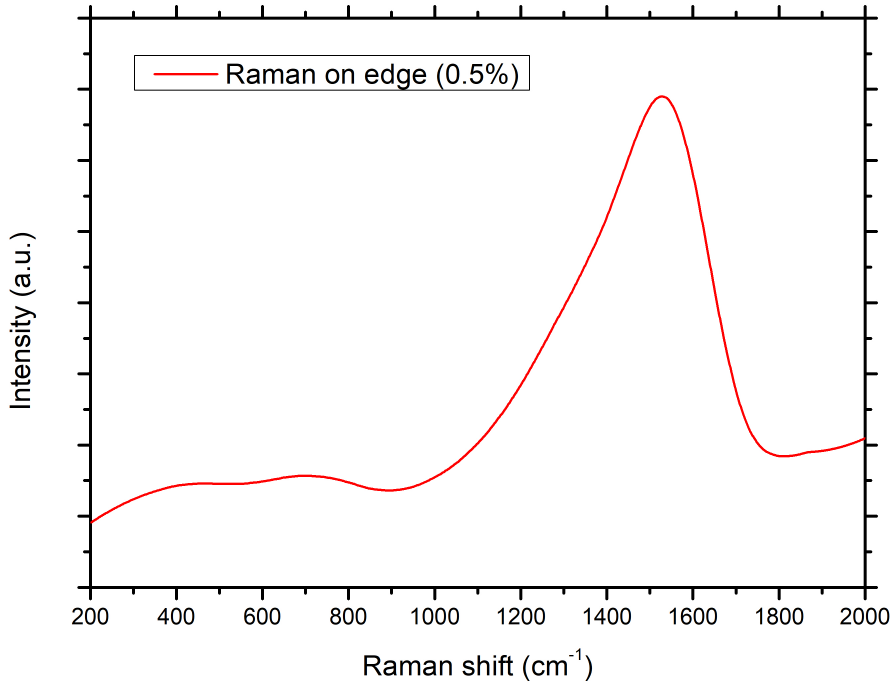

Figure 3.4: Raman spectrum of DLC coated tools with 0.5% of nominal power value

indicative of a good adhesion to the substrate.

Due to lack of available time, the DLC coated tools were not included in the initial experimental array but secondary test were done in order to benchmark those coatings with two variable thicknesses against the coatings tested initially. However, the novel deposition protocol established for coating of micromilling tools is a novel output of this work as it needs a very careful parametrisation. It may be noted that when the existing coating protocol and optimised parameters for coating of macromachining tools was used for the microtools, the coating failed.

3.2 Design of Experiments

Before attempting machining trials, a design of experiment was conducted using Taguchi's approach described in Chapter 2.4 in order to engage in a multiple output optimisation process. The average roughness (Ra), specific cutting energy (SCE) and material removal rate (MRR) were the parameters optimised for varied input parameters like feed rate (f), spindle speed (SS) and tool coating. It was decided to run the experiments at three different levels for three factors (table 3.1). The parameters present in the table were extracted from literature as discussed in Chapter 2.3. Since our limitation lies in the diameter of the milling tool of 200 μm, the parameters were chosen in a manner to explore the parameters space found in literature for that diameter size. For example, the depth of cut found in literature varied between 10 μm and 30 μm mostly using a tool with 150 - 250 μm diameter. The minimum number of experiments to be conducted calculated using *DOF* would be:

$$DOF = 1 + 3(3-1) = 7 \tag{3.1}$$

The appropriate orthogonal array would be an L9 array as confirmed by table 2.5 and it is presented in table 3.2.

Table 3.1: Levels and Parameters selected

Parameter	**Level 1**	**Level 2**	**Level 3**
Spindle speed (rpm)	20000	25000	30000
Feed rate (mm/min)	50	75	100
Coating type (nm)	no coating	HM (TiAlN based)	UT (TiCN based)

Table 3.2: L9 Experimental Array

Experiment number	Inputs		
	Feed rate (mm/min)	SS (rpm)	Tool Coating
1	50 (L1)	20000 (L1)	no coating (L1)
2	50 (L1)	25000 (L2)	UT (L3)
3	50 (L1)	30000 (L3)	HM (L2)
4	75 (L2)	20000 (L1)	UT (L3)
5	75 (L2)	25000 (L2)	HM (L2)
6	75 (L2)	30000 (L3)	no coating (L1)
7	100 (L3)	20000 (L1)	HM (L2)
8	100 (L3)	25000 (L2)	no coating (L1)
9	100 (L3)	30000 (L3)	UT (L3)

3.3 Milling Strategy

The milling strategy employed in this project is linear ramp milling. By definition, linear ramp milling is a strategy that does not require a starter hole, it ramps into the block removing material following an incremental depth. Given the Titanium samples' dimensions and locations of fixating holes, it was decided to machine an area of 50 x 30 mm^2 to have sufficient clearance from the fixating holes.

The sloped depth linear equation was calculated and extrapolated in order to set the tool's starting point outside of the block.

$$a_p = z = ay + b \tag{3.2}$$

with $y = 0$, $a_p = -0.015$
and $y = 30$, $a_p = -0.005$
This results in the equation being:

$$a_p = \frac{1}{3000} y - 0.015 \tag{3.3}$$

Then, the extrapolation is done for an a_p value of 0.016 mm which results in $y = -3mm$ as initial position for the tool. Now the machining code can be written as:

BEGIN PGM TRIAL01 MM
BLK FORM 0.1Z X-20 Y-10 Z-10
BLK FORM 0.2 X+20 Y+10 Z+0
TOOL CALL 5 Z S20000
M3 M7
Q1 = 7
LBL1
L X+Q1 Y-3 Z-0.016 F50
L X+Q1 Y+30 Z-0.005 F50
L Z+20 FMAX
Q1=Q1+0.15

CALL LBL1 REP371

M30

END PGM TRIAL01 MM

———————————————————-

The tool path is presented in figure 3.5.

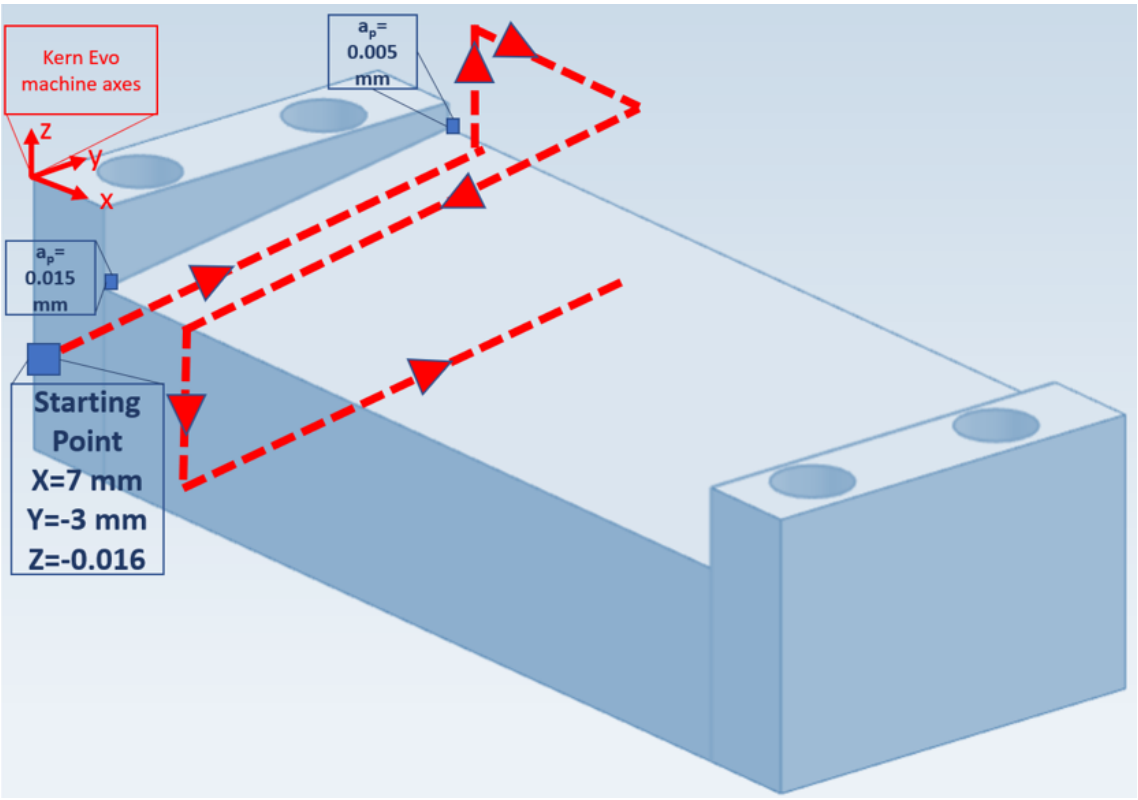

Figure 3.5: Machining tool path

3.3.1 Machining Calculations

The material removal rate using the following equation:

$$MRR(\frac{mm^3}{min}) = \frac{V}{t} \tag{3.4}$$

where V is the volume of the machined area, t is the machining and overlap movement time. To calculate specific cutting energy, the resultant cutting force (F_R) needs to be calculated and the following equations used:

Cutting Speed (V_c)

$$V_c(\frac{m}{min}) = \frac{\pi D_{tool} SS}{1000} \tag{3.5}$$

where D_{tool} is the nominal tool diameter, SS is the spindle speed (rpm).

Resultant Force (N)

$$F_R(N) = \sqrt{F_t^2 + F_n^2} \tag{3.6}$$

where F_t is the tangential force and F_n is the normal force.

Specific Cutting Energy (SCE)

$$SCE(\frac{J}{mm^3}) = \frac{V_c F_R}{MRR} \tag{3.7}$$

3.4 Experimental Set-up

The Kern Evo machine (figure 3.6) used in this thesis runs on the Heidenhain machining code. The machining code consists of a list of several instructions/blocks, each written on a separate line, to be performed in the order they are written. In order to promote safety, predictability and readability, it is very important to adhere to a standard structure for the sequence of the blocks' arrangement. The generic machining code used in this experiment was presented in part 3.2. Prior to starting the machining process, the sample was mounted, levelled by using skimming the surface and probed to define the origin of the axes system. In addition, a Mahr Millimar probe was used to make sure that the sample is mounted straight. The measurement set up can be seen in figure 3.7.

In the micromilling experiments, air cooling was used.

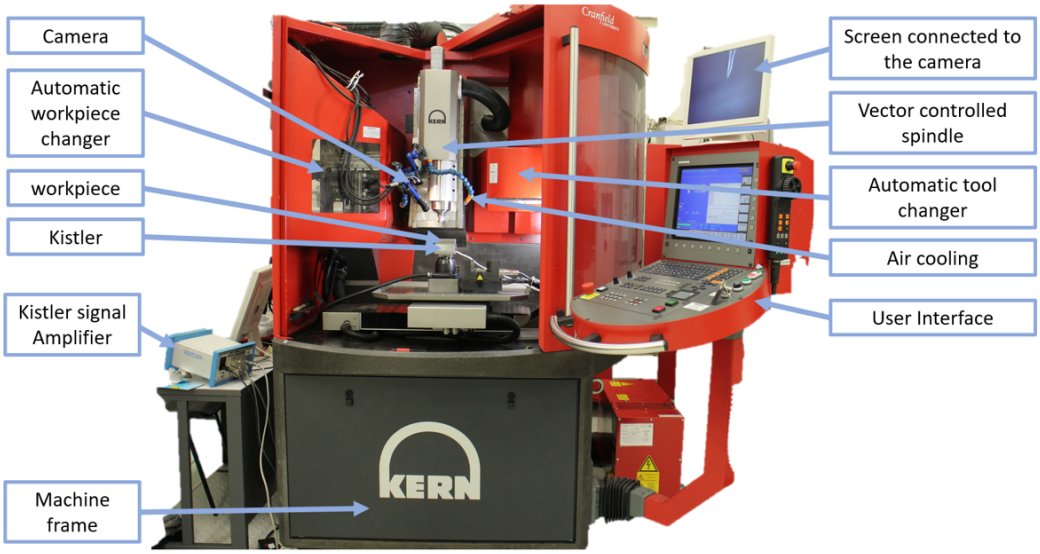

Figure 3.6: The Kern EVO micromilling machine in Cranfield University, B70

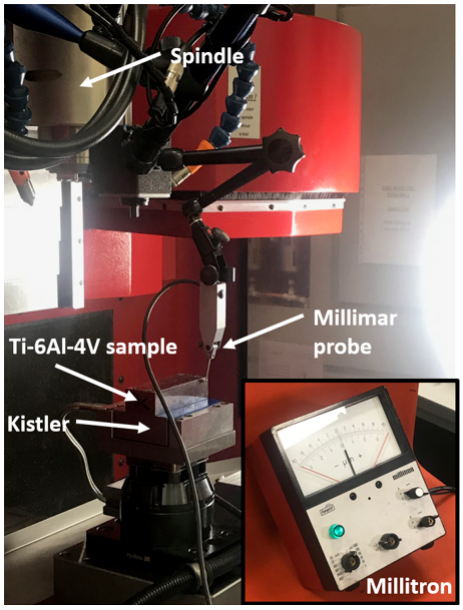

Figure 3.7: The millimar probe with the millitron indication instrument

3.4.1 Dynamometer - Cutting Forces Measurement System

The Kistler minidyn 9256C was used to measure the cutting forces. It was mounted on the the Kern evo machine bed as shown in figure 3.8. The dynamometer was calibrated by setting known weights of 17 g, 0.5 kg and 1 kg on it and applying corrections based on the difference between the measured force and the calculated force in the Z direction.

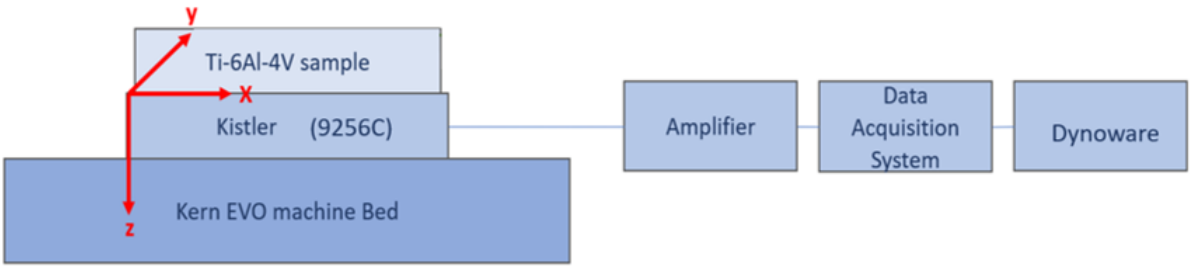

Figure 3.8: Dynamometer set-up

3.4.2 Roughness Measurements

Roughness can be evaluated using various parameters depending on the application. In literature, researchers have mostly been using the arithmetic roughness value (Ra) in order to evaluate the surface quality in experimental work and simulation [80] [81]. In addition, researchers have studied bacterial response/bacterial adhesion on surfaces with Ra as surface measurement [82].

The roughness (Ra) was measured using the coherence scanning interferrometer shown in figure 3.9 (Taylor Hobson CCI6000) across the direction of lay at 4 positions which are the 4 edges of the machined area as shown in figure 3.10.

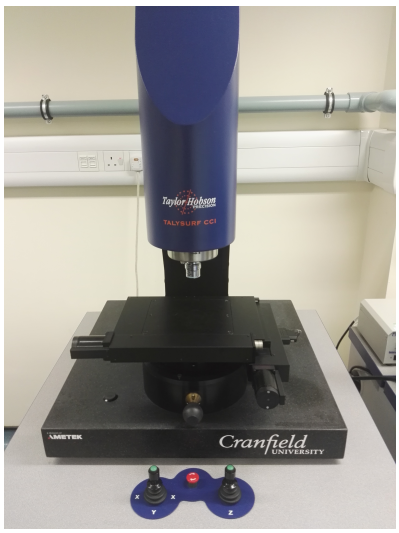

Figure 3.9: Taylor Hobson CCI6000

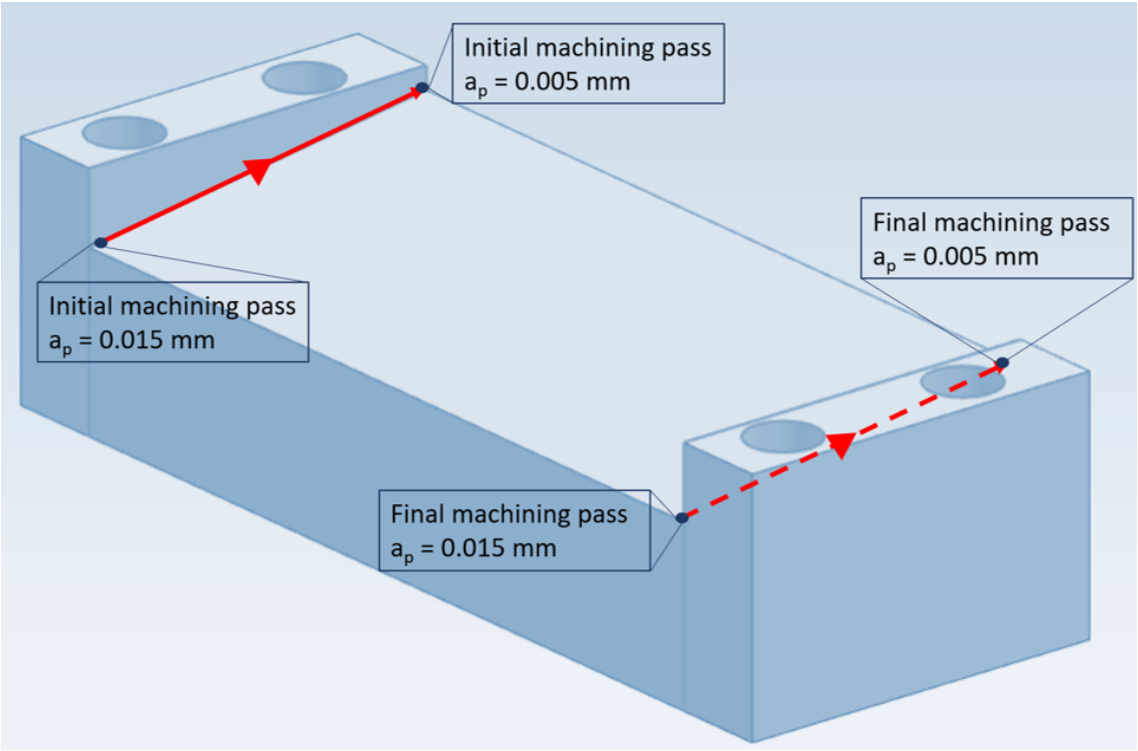

Figure 3.10: Roughness measurement areas

3.4.3 Form Measurements

The form of the surface was measured using a Polytech TopMap TMS-500 shown in figure 3.11.

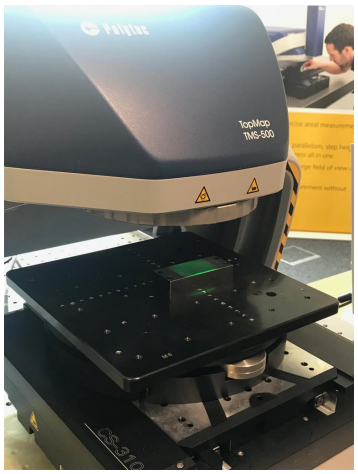

Figure 3.11: Polytech TopMap TMS-500

3.4.4 Material Characterisation Methods

A Tescan Vega SEM was used to obtain images of the tools prior to machining. The tool for the first trial was imaged using an XL30 FEI before Tescan Vega was procured. Images of the tools after machining were obtained using a Tescan LYRA SEM due to availability. The elemental analysis of the tools and their coatings was done using an EDS integrated in the Tescan LYRA SEM. The DLC coated tools were characterised by Raman spectroscopy with 532 nm wavelength at different power levels (0.5, 1 and 5% of the nominal power value).

Chapter 4

Results and Discussion

4.1 Characterisation of tools Pre and Post-machining

The micromilling tools were screened in order to evaluate their quality and sharpness. It should be noted that several uncoated tools were observed to not be sharp when inspected visually as they had severely eroded cutting edges (figure 4.1) thus they were removed from the lot and not used in the trials.

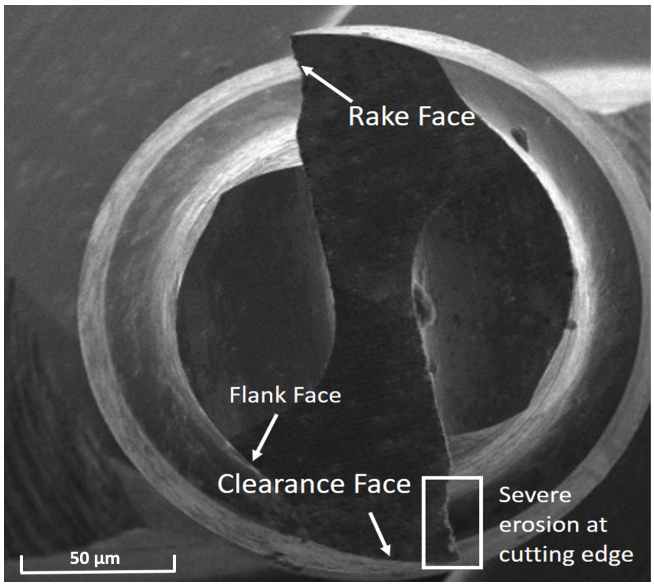

Figure 4.1: Severely eroded uncoated tool cutting edge

SEM images of the tools from trial 1, 2 and 3 prior to machining are shown below. The rest of the trials' tools' SEM images can be found in the appendix infromation given at the end of this dissertation.

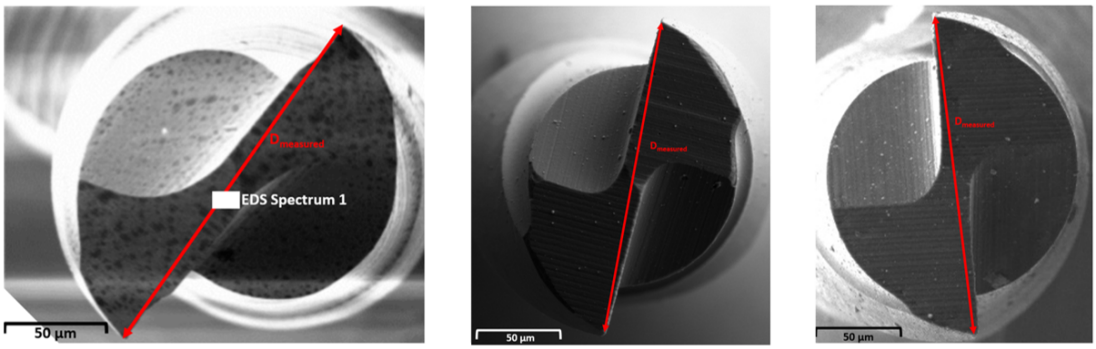

Figure 4.2: SEM Images of Tool (a) 1 (b) HM from trial 21 (c) UT from trial 3 with annotations

Tool diameters measured with imageJ software are tabulated in table 4.1 and the histogram showing the weight percentage distribution obtained from EDS corresponding to the tool shown in figure 4.2 (a) is presented in figure 4.3.

Table 4.1: Tools used for each trial along with their diameters

Trial number	Feed rate (mm/min)	SS(RPM)	Coating	Tool number	Diameter(mm)
1	50	20000	No	1	0.181827
2	50	25000	HM	HLS1	0.188382
3	50	30000	UT	CES1	0.184804
4	75	20000	HM	HLS2	0.186886
5	75	25000	UT	CES2	0.187323
6	75	30000	NO	2	0.189558
7	100	20000	UT	CES3	0.185665
8	100	25000	NO	3	0.19181
9	100	30000	HM	HLS3	0.185493

As a first step to characterising the coatings, the coated tools were ultrasonically cleaned in acetone and EDS analysis was performed on them. The results for the tool with TiAlN based coating (HM) are presented in figure 4.4. For the tool coated with TiCN based coating (UT), the SEM image and EDS results are shown in figure 4.6.
In an attempt to determine the coating thicknesses, an HM coated (TiAlN based) tool and a UT coated (TiCN based) tool were mounted in resin, ground and polished to reveal their cross-sectional areas (destructively tested). A thin layer of gold (i.e.10 nm) was sputtered on the resin mounted samples.This provides a conduction path which allows the imaging

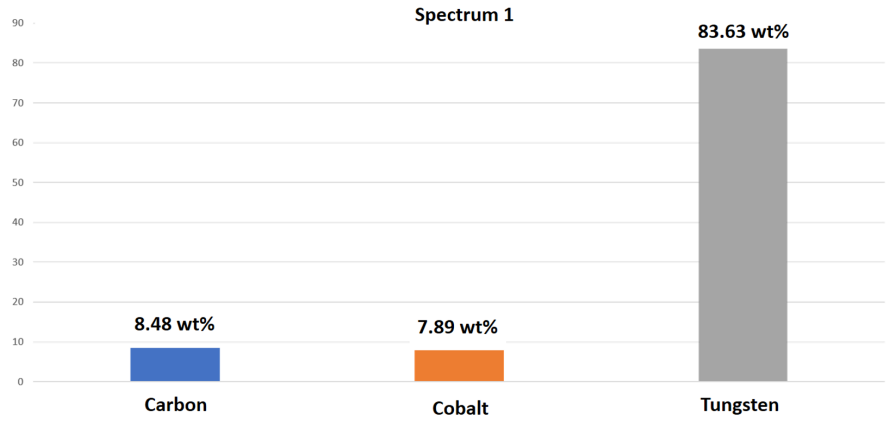

Figure 4.3: EDS measurement revealing weight percent of atoms in the uncoated micromilling cutting tool

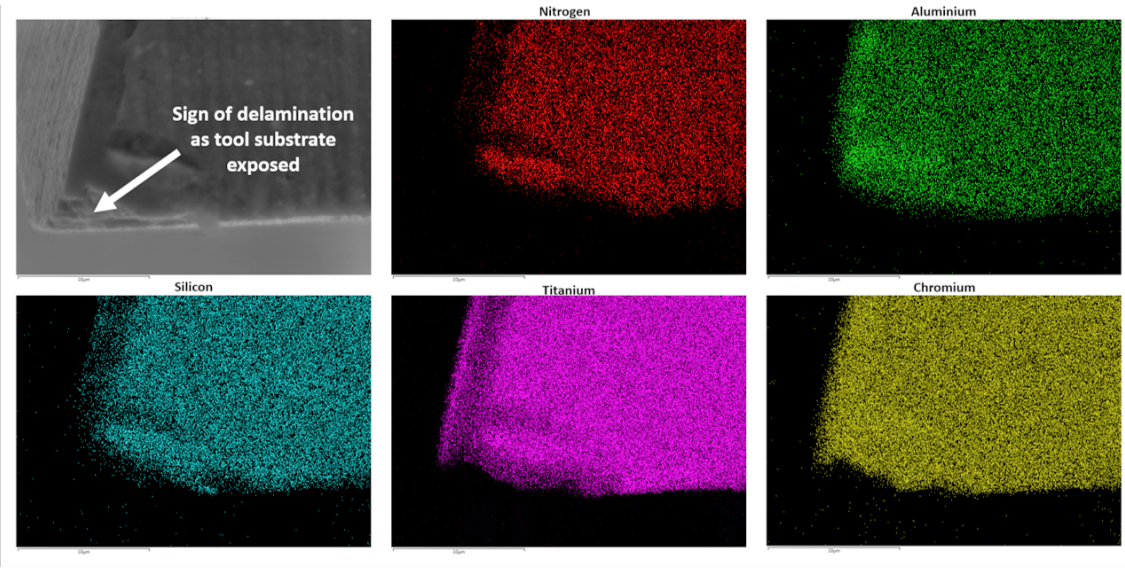

Figure 4.4: EDS map of tools coated with a TiAlN based coating (HM coating)

of these samples at high voltages, thus high resolution (small effective beam diameter). In addition, it provides a higher secondary electron yield which improves the signal to noise ratio in imaging.

EDS analysis was conducted on these samples in order to reveal their coatings elements and quantify their thicknesses. These results for the HM and the UT coated tools are shown in figure 4.4 and figure 4.7. The presence of vanadium could be attributed to the fact that the titanium target used in the coating deposition process (PVD) was not a pure titanium as vanadium is a very common alloying element for titanium. Another hypoth-

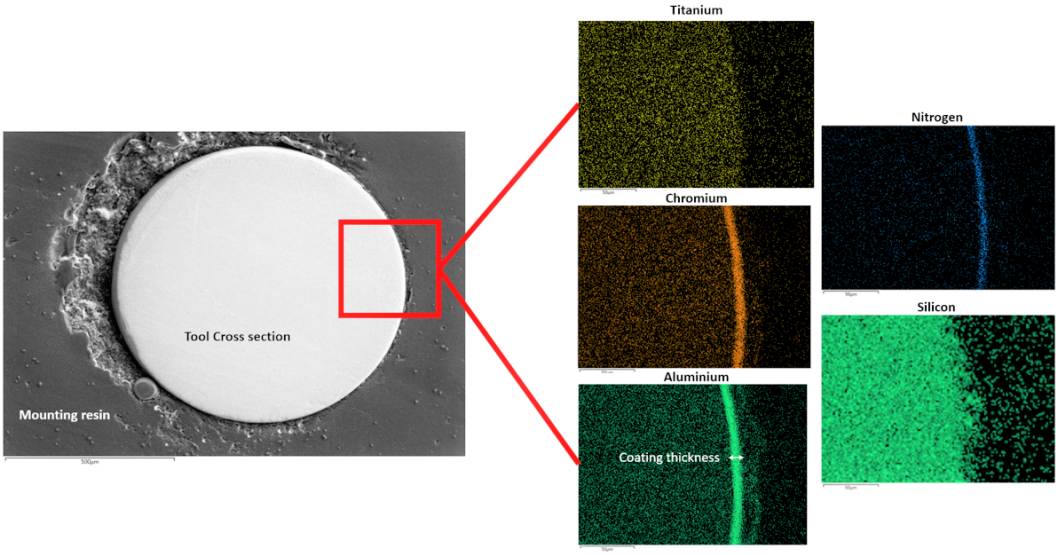

Figure 4.5: Cross-sectional imaging and EDS mapping of HM coated tool (TiAlN based)

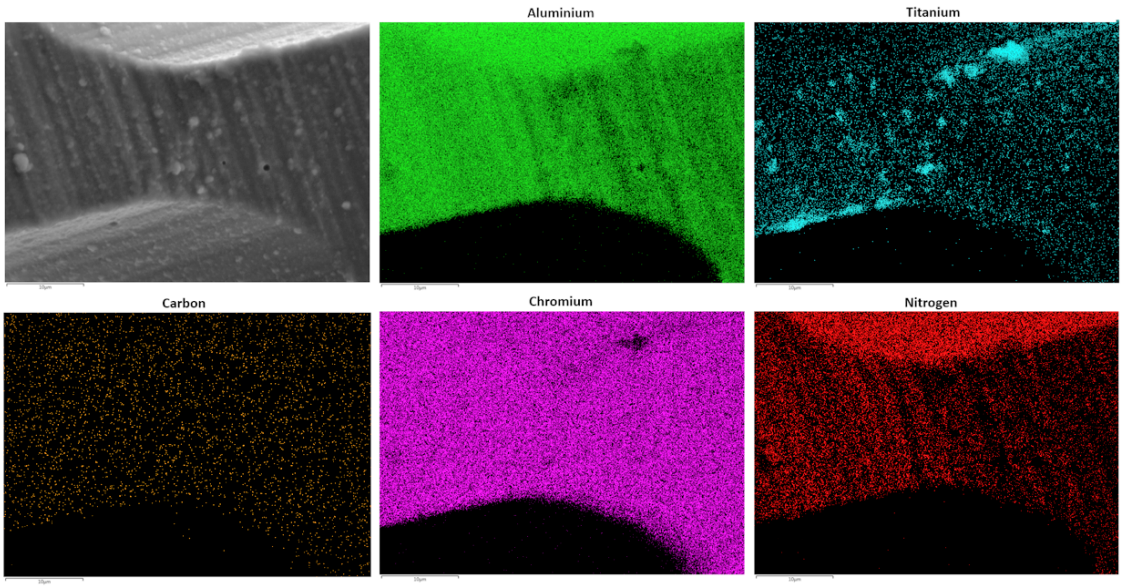

Figure 4.6: SEM image and EDS map of the UT tool coating elements (UT: TiCN based coating)

esis would be that the software automatic ID attributed the peak at to Vanadium but in fact it is an oxygen peak which is explained more in table 4.2. This problematic peak attribution occurs generally for constituents present at minor ($0.01 \leq \text{Cr} \leq 0.1$) and trace ($\text{C} \leq 0.01$) levels. In this case, the concentration of this element is less than 0.02 which

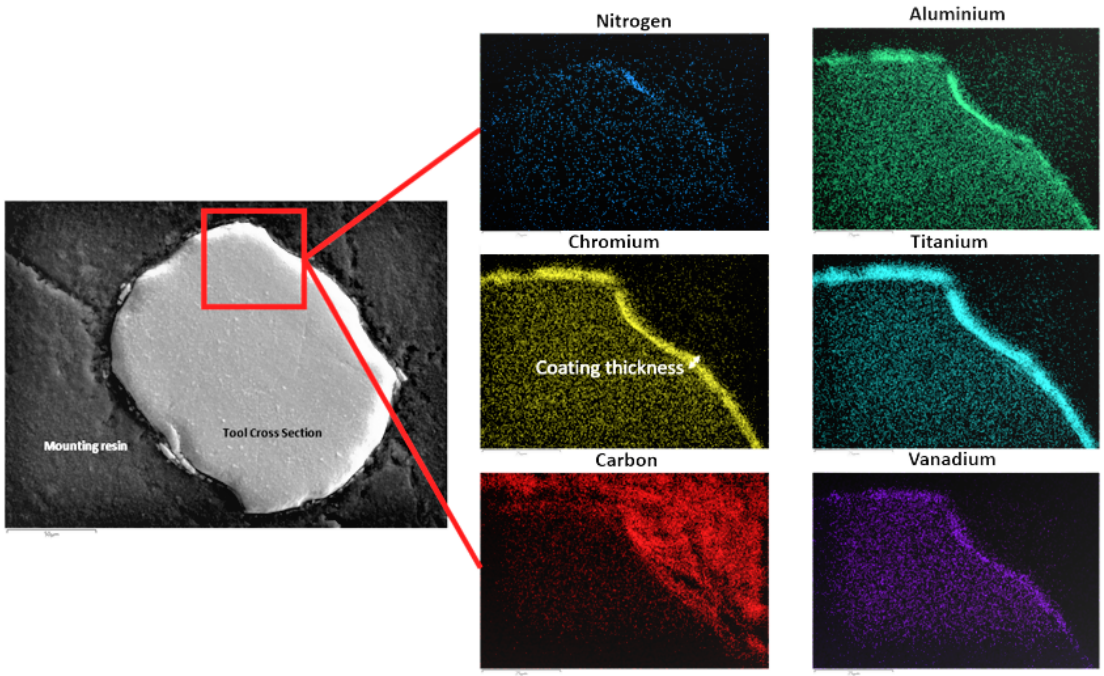

Figure 4.7: Cross-sectional imaging and EDS mapping of UT coated tool (TiCN based)

could mean that in fact there is an absence of Vanadium. As for the presence of Silicon, it can also be attributed to the same peak identification problem in the automatic ID of the processing software. Table 4.2, shows the possible elements that could be identified as Silicon in low concentrations. The element that is most probably present in this case would be tungsten (W) as the tools are made of Tungsten carbide.

Table 4.2: Automatic peak identification problem regions[83]

keV	
0.510 - 0.525	O K (0.523) and V L_α (0.511)
1.69 - 1.80	Si Ka (1.740); Rb L_α (1.694); Sr L_α (1.806); T_α M_α (1.709); W M_α (1.774)

For the HM coated tool, the manufacturer has specified a hardness of 3500 to 4000 Vickers.

Table 4.3: Hardness of different coating systems found in literature.

Coating	Hardness (Vickers)	Reference
TiAlN	2850	[62]
TiAlN/TiSiN	3500	[62]
TiAlN/CrAlN	3800	[62]
TiAlCrN	3500	[59]
TiCN	2500-2800	[84]
Ti/TiCN/TiAlCrN	3900	[85]
TiAlN/CrSiN	3300-3600	[86]

If we compare this range with coating hardnesses found literature (table 4.3), we can hypothise that the coating system is possibly TiAlN/CrAlN. The measured thickness of the coating system is around 6 μm. As for the UT coating, it is specified that the hardness ranges from 3000 to 3500 Vickers.

That combined with hardness values found in literature hints to conclude that the coating system is most probably TiCN/TiAlCrN. The measured thickness of the coating system was around 4 μm.

In conclusion, the EDS analysis showed that the two commercially used tools based on the two undisclosed coating types (herein referred as HM coating and UT coating) were TiAlN/CrAlN coating (HM coating) having thickness of about 6 μm whilst the UT coating was based TiCN/TiAlCrN with a thickness of about 4 μm. After machining, images of the tools were taken with an SEM. The uncoated tool used in trial 1 was the only uncoated tool that survived the trials and did not fracture. It shows signs of flank wear and edge corner rounding as seen in figure 4.8 (a). On all the tools, post-machining, there is presence of workpiece material adhered to the cutting edge as shown in figure 4.10. This material can be considered a built-up edge (BUE). However, the amount of BUE observed on the uncoated tool is more than that observed on coated tools. This finding is in line with the research done by Ucun *et al.* [87] in which they investigated the BUE effect on surface finish of Inconel 718 alloy while micromilling with different process parameters and observed that machining with a coated cutting tool minimises the formation of BUE. It is expected that BUE will play a role in the roughness measurement as it changes the effective tool geometry as shown schematically in figure 4.9.

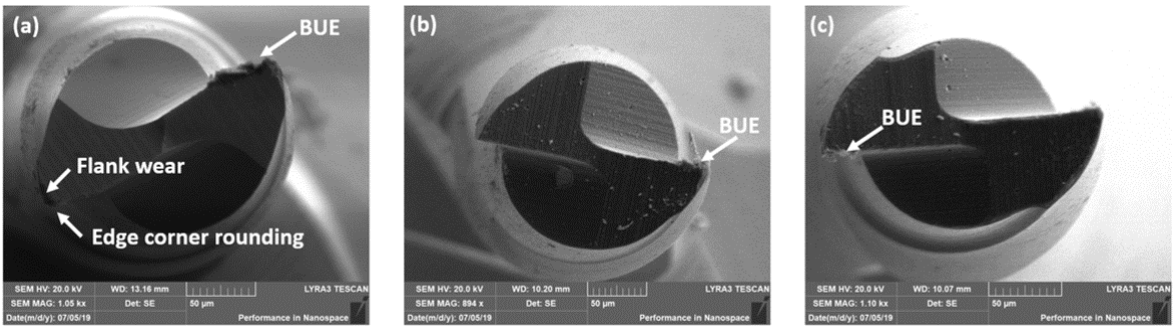

Figure 4.8: SEM imaging of tools after machining: (a) Uncoated tool (b) UT coated tool (c) HM coated tool

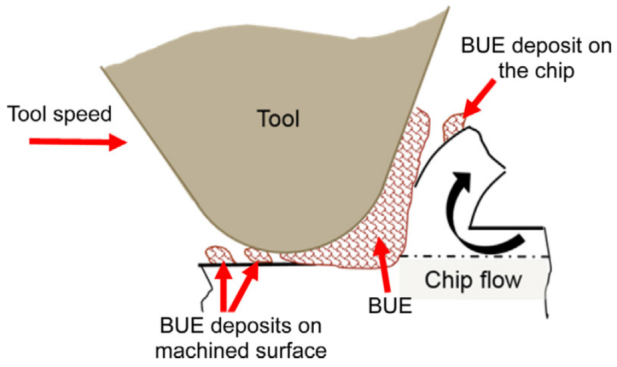

Figure 4.9: Schematic diagram of built-up edge formation in micro machining processes [88].

Qualitative analysis of figure 4.10 showed that UT coated tools had more amount of BUE. That could be attributed to adhesion and cohesion between the workpiece material (Ti-6Al-4V) and the tool coating elements (TiCN/TiAlCrN) [87]. Because of strong adhesion of BUE, the measurement of wear of tools post-machining could not be done reliably.

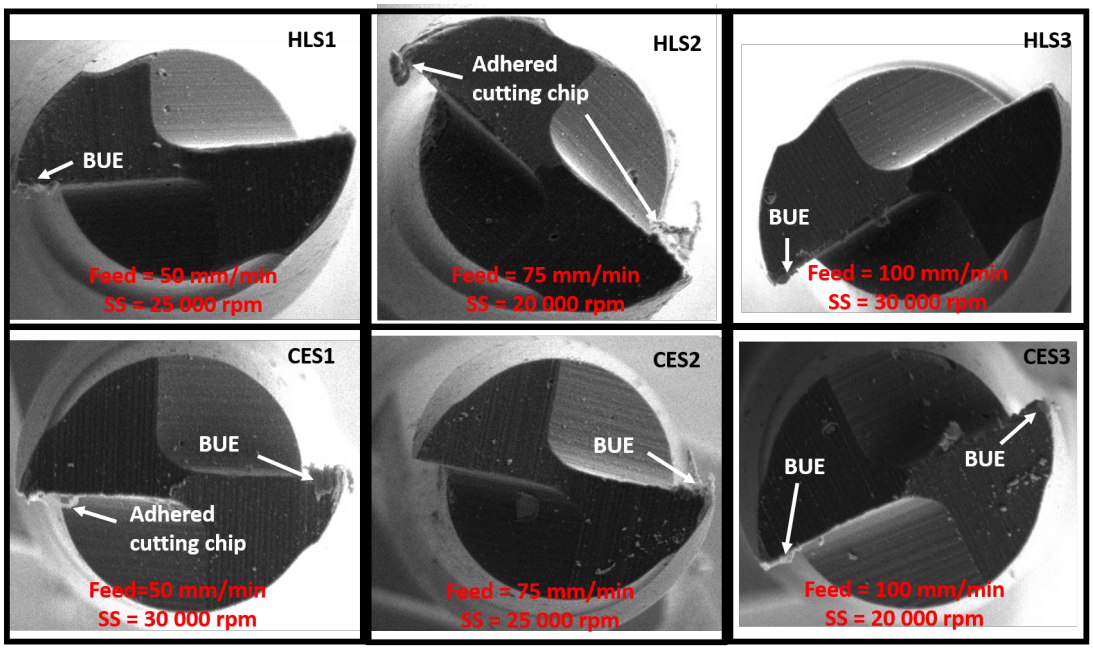

Figure 4.10: Coated tools after machining

4.2 Force Measurements

One major issue in measuring the force for ultraprecision machining is the post-processing of the data obtained. As the forces are very small, external sources can add noise to the measurement data. To remove this noise low pass filters are used with cut off frequencies of the filters depending on whether dynamic influences of the unbalances are of interest or not [89]. As shown in figure 4.11, the unfiltered force signal is very noisy and hardly any pattern can be discerned.

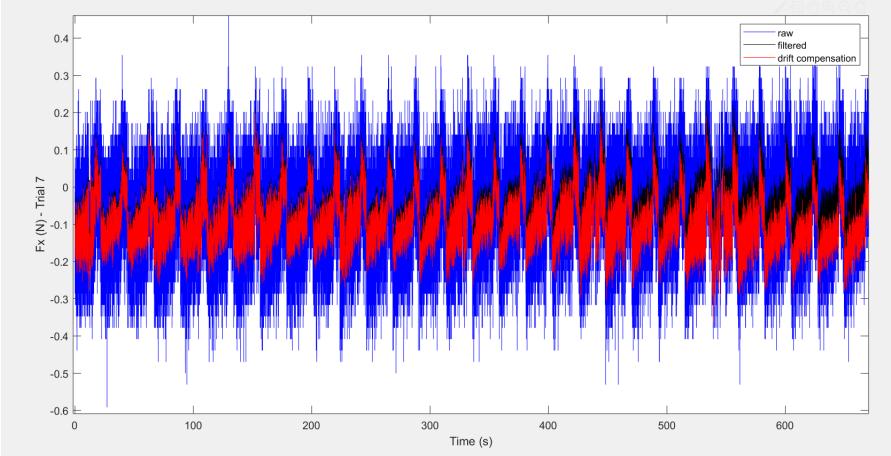

Figure 4.11: Raw, Filtered and drift compensated F_x data from Trial 7

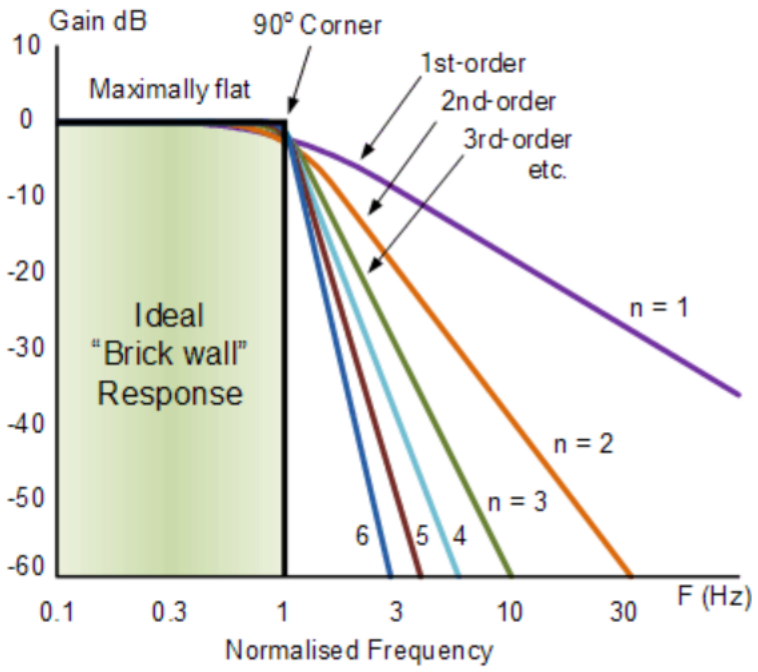

Figure 4.12: Butterworth filter with different orders [90]

The butterworth filter was applied in this case to render the force data clearer. The butterworth filter is a low pass filter which is dependent on two parameters; the order (n) and the cut-off frequency (f_c). The bigger the order, the higher the reduction in magnitude of high frequency signals. Figure 4.12 shows how the order influences the gradient of the curve. Signals with frequencies below the cut-off frequency pass whereas signals with higher frequencies are attenuated. On one hand, the cut-off frequency has to be less than the sampling frequency, which is 100 Hz, to avoid noise affecting the results. On the other hand, it has to be high enough to preserve the useful force data needed to carry out the analysis. Therefore the cut-off frequency was chosen as 10 Hz. In addition, drift compensation was applied by fitting a polynomial to the force data and then extracting that polynomial from the data.

A schematic of the forces exerted on the tool is presented in figure 4.13. This will help in understanding the recorded forces and their directions (negative or positive).

From this schematic, F_x and F_y are expected to be negative and F_z is expected to be positive. In addition, the magnitude of the forces is expected to be bigger when the cut starts, as it starts at a depth of 15 μm, and decrease as the depth of cut decreases to 5 μm as shown in figure 4.14 (a). In figure 4.14 (b), the recorded forces are presented. In

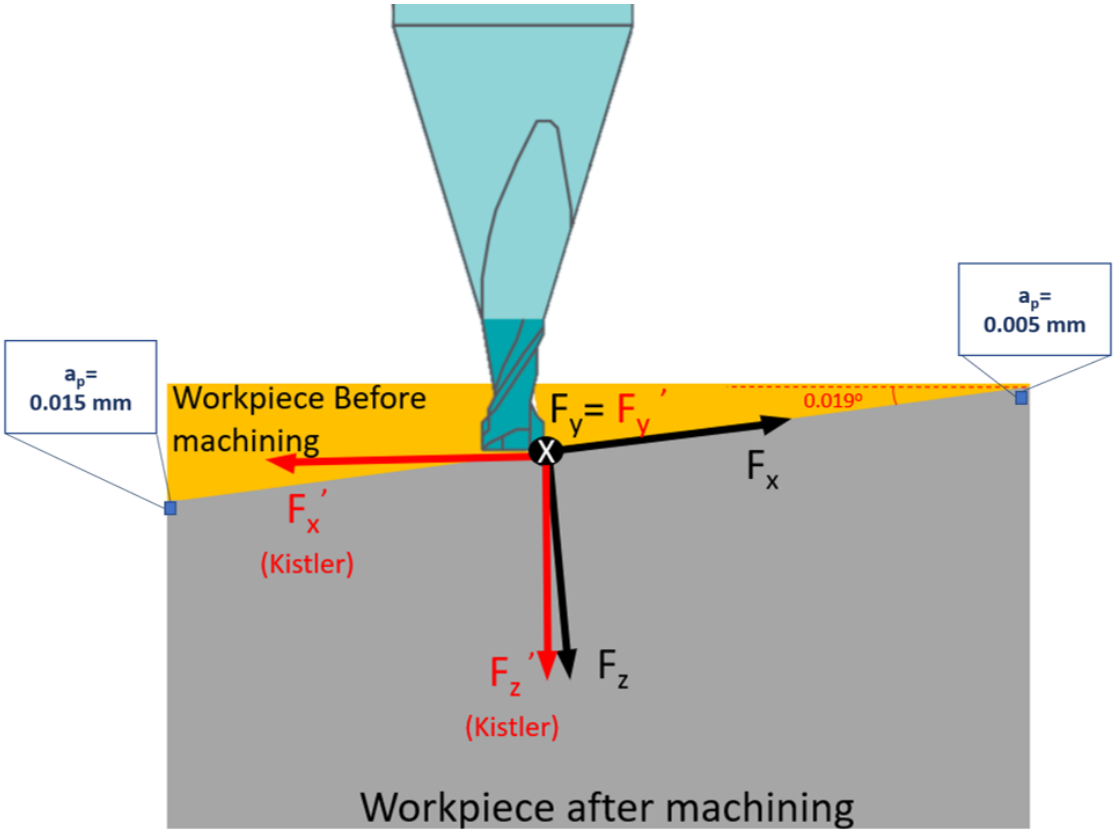

Figure 4.13: Schematic of forces exerted on the tool as it cuts and the axes of the kistler dynamometer.

calculating the resultant force, the slope of the machined area has to be taken into account:

$$F_R = \sqrt{(F_x cos\theta)^2 + (F_y cos\theta)^2 + (F_z cos\theta)^2} \tag{4.1}$$

where θ= 0.019^o. The resultant forces were calculated for each machining pass and then averaged to obtain the final resultant force tabulated in table 4.2. Cutting forces contain important information on the mechanics and dynamics of the machining processes and are directly related to the power consumed while the tool is cutting through the material. Therefore, the specific cutting energy can be calculated (table 4.15).

Minimising the SCE is the goal in any mechanical material removal process in order to minimise the consumption of energy per volume of material removed. Consequently, a particular attention is given to the lowest mean SCE values for each input parameter level. In terms of feed rate, level 2 (75 mm/min) possesses the lowest mean SCE.

For the different spindle speed levels, level 1 (20,000 rpm) gives the lowest mean SCE.

And finally, HM coating (TiAlN based) of level 2 presented lowest mean SCE between the different coating levels.

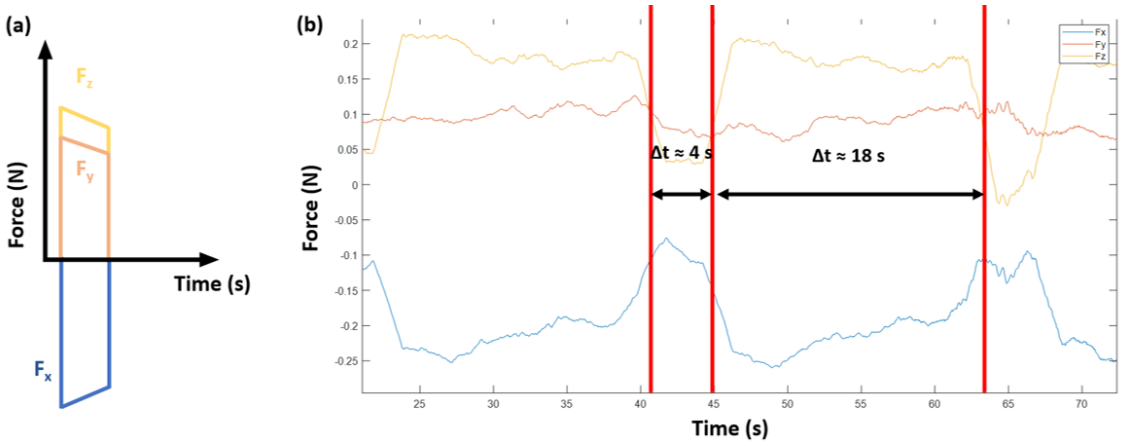

Figure 4.14: Force Vs Time (a) expected trend (b) recorded from trial 7

From figure 4.15, the influence of each input parameter level on SCE can be inferred. The feed rate and spindle speed are shown to influence SCE the most as the differences in the mean SCE values from one level to another for both these parameters are big. To better understand the influence of feed rate on SCE. Trials 1, 4 and 7 can be taken as examples. These trials have the same spindle speed values (SS level 1) so the influence of the SS is ignored. By observing the results of these trials, it is shown that as feed increases, force increases. Theoretically, as force increases SCE increases too. However, since the feed rate is also increasing then the influence of the MRR=fn(f) on SCE comes into play too. What governs SCE, in this case, is be the parameter that is inducing the biggest percent of variation. In this case it is MRR thus the feed.

This explains the fact that as feed is increasing SCE is observed to be decreasing. However, there is an exception that is found in level 2 of SS more specifically, more specifically trial 8 of that level. When the feed rate is increased from 50 mm/min to 75 mm/min, SCE is still mostly influenced by the MRR. However, the increase in the percentage of variation of the resultant force (148 %) as feed increases from 75 to 100 mm/min dominates over the variation in feed (33%) or MRR. Thus SCE in this case increases. This huge increase in the percentage of variation of the resultant force can be directly linked to the tool being uncoated and not very sharp therefore undergoing higher forces.

In terms of spindle speed, trials 1 to 3 can be taken as examples. As SS increases, the force decreases. Since SCE is a function of both V_c=fn(SS) and F_R, then the parameter that governs wether it increases or decreases would be, again, that which causes the biggest percentage in variation which in this case is V_c thus SS. Therefore, SCE is increasing with SS.

The presence of tool coating has a big impact on SCE although tool coating type does not seem to affect it greatly. This impact could be attributed not only to the presence of coating but also to the fact that the uncoated tools used were not as sharp as the coated ones used. Cutting edge geometry and sharpness have a very big impact on SCE. For instance, tool wear increases SCE and renders the process less energy efficient. Further discussion about the influence of the input parameters on SCE and correlations between SCE and Ra are presented in Chapter 4.5. The error bars presented in figure 3.7 are

Trial nb	Feed rate (mm/min)	SS (RPM)	Tool Coating	F_R (N)	SCE (J/mm^3)
1	50 (L1)	20000 (L1)	No (L1)	0.21884	36.8025
2	50 (L1)	25000 (L2)	HM (L3)	0.21763	45.7487
3	50 (L1)	30000 (L3)	UT (L2)	0.21711	54.7673
4	75 (L2)	20000 (L1)	HM (L3)	0.2014	22.6379
5	75 (L2)	25000 (L2)	UT (L2)	0.18233	25.618
6	75 (L2)	30000 (L3)	No (L1)	0.26361	44.1467
7	100 (L3)	20000 (L1)	UT (L2)	0.26221	22.162
8	100 (L3)	25000 (L2)	No (L1)	0.45659	47.4503
9	100 (L3)	30000 (L3)	HM (L3)	0.24432	30.9749

stemming from the difference between the nominal size of the tools and actual measured diameters.

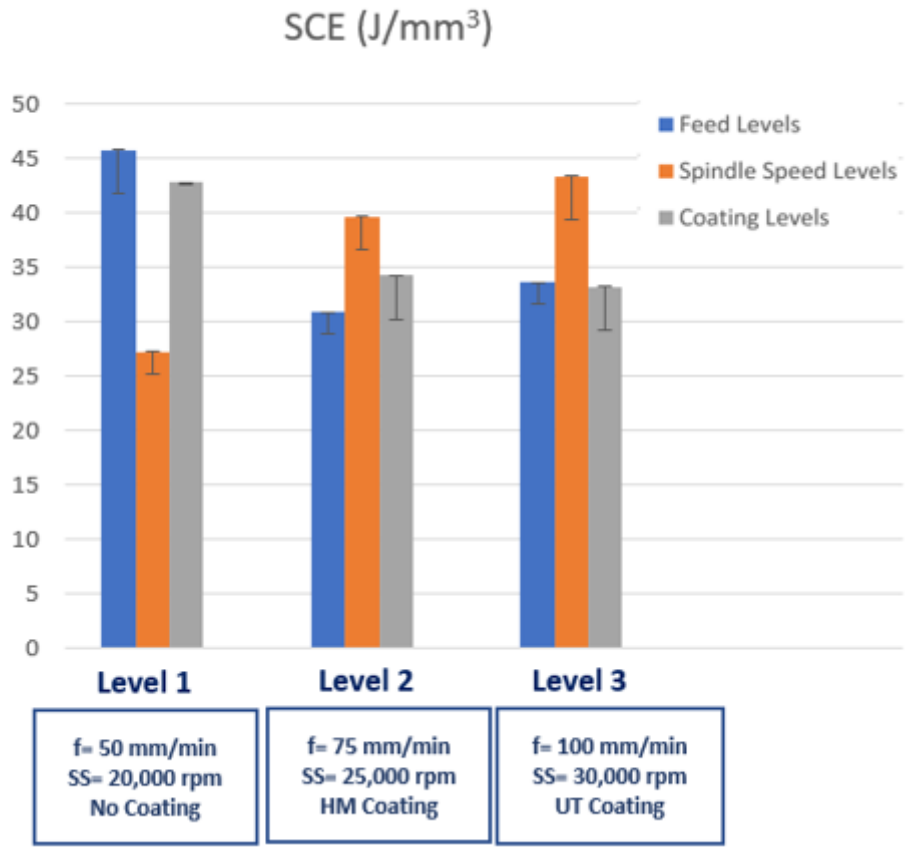

Figure 4.15: Histogram of the SCE classed according to different levels for each input parameter

4.3 Roughness measurements

Roughness measurements taken at 4 locations for each sample were averaged and are presented in table 4.4. The tools used in trials 6 and 8 failed before the machining was completed (figure 4.16). Roughness data was still collected on all the samples as described in chapter 3.

Roughness data shows that the roughness value is the highest in trial 6 where an uncoated tool was used along with Level 2 feed rate and spindle speed. In contrast, the lowest roughness is presented in trial 2 where the feed was at level 1, spindle speed was at level 2 and the tool used was coated with HM, the TiAlN based coating.

In the micromilling process, surface roughness vary depending on the feed rate, cutting edge radius and cutting tool entering angle. Experimentally, the actual surface roughness is significantly affected by in-process tool wear at the time of manufacturing, the

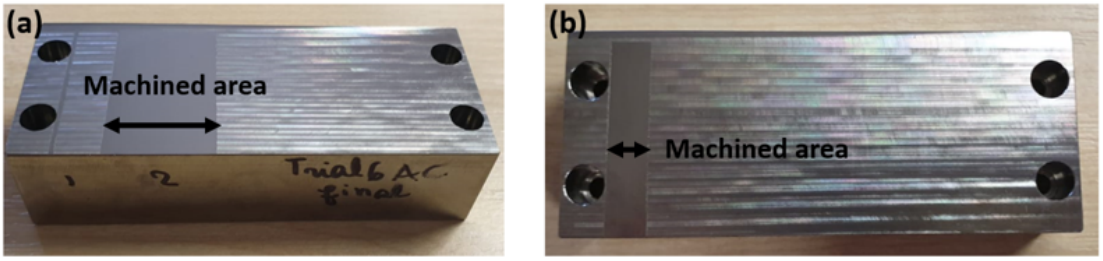

Figure 4.16: Samples of trials (a) 6 and (b) 8.

Table 4.4: Roughness Measurements for each trial sample

Trial number	Feed rate (mm/min)	SS (RPM)	Tool Coating	Ra (μ m)
1	50 (L1)	20000 (L1)	no coating (L1)	0.153018
2	50 (L1)	25000 (L2)	HM (L3)	0.092059
3	50 (L1)	30000 (L3)	UT (L2)	0.202293
4	75 (L2)	20000 (L1)	HM (L3)	0.094742
5	75 (L2)	25000 (L2)	UT (L2)	0.39338
6	75 (L2)	30000 (L3)	no coating (L1)	0.452465
7	100 (L3)	20000 (L1)	UT (L2)	0.16557
8	100 (L3)	25000 (L2)	no coating (L1)	0.346791
9	100 (L3)	30000 (L3)	HM (L3)	0.183777

dynamics of the machining conditions and the stiffness of tool-workpiece contact.

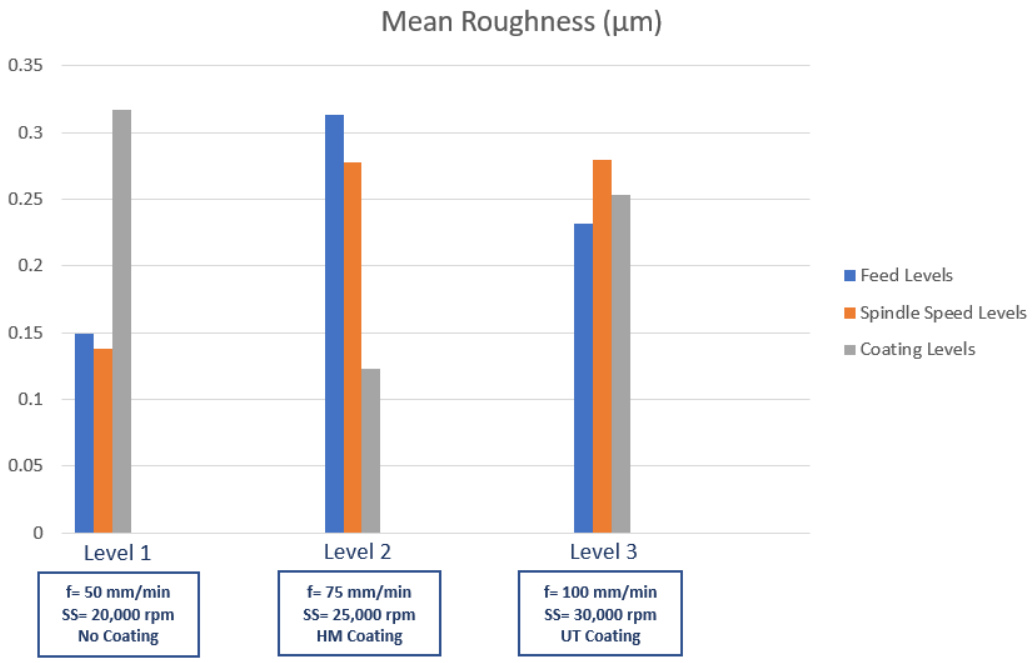

Figure 4.17: Histogram of mean roughness classed according to different levels for each input parameter

Figure 4.17 shows the impact each input parameter has on the roughness for each of the three levels. It is evident that all input parameter play a big role in the output roughness value; low feed and low spindle speed along with HM coated tool showed lowest roughness values. The impact of the tool coating seems to be the highest as the discrepancies in roughness values from level to level are the biggest.

4.4 Form Measurements

In order to evaluate the stability of the machine tool, the form of the machined sample was measured and used to obtain the slope of the inclined machined area. A representation of the form of one of the titanium machined samples (trial 7) is shown in figure 4.18. After measuring the slope of all the samples, it was noticed that the change in feed was the most influential parameter as opposed to change in spindle speed. Figure 4.19 presents the average slope error calculated between the target slope and the measured slope for each feed level. It shows that as the feed increases, the error decreases and stability as

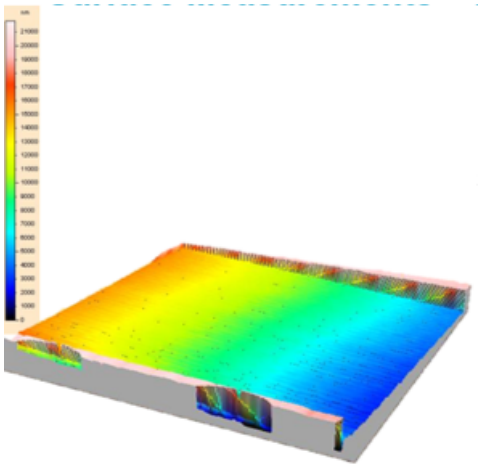

Figure 4.18: Axonometric representation of the form of the machined titanium sample from trial 7

well as precision increases, a fact that has been previously investigated to be enhaced especially in the case of micromilling [91].

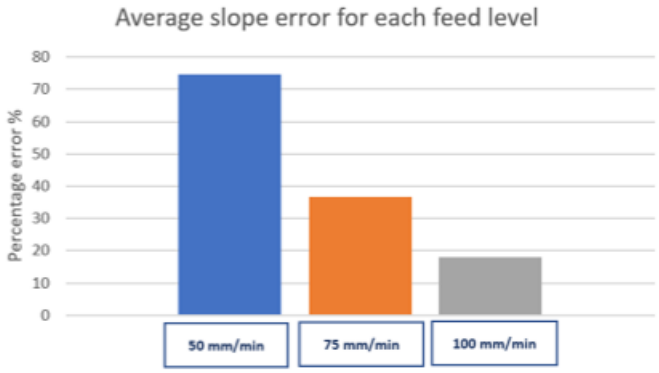

Figure 4.19: The average slope error for each feed level

4.5 Material Removal Rate

The material removal rate for each trial was calculated using the equation presented in chapter 3 and presented in table 4.5. Since in trial 6 and 8, the tools could not machine the entire area, the material removal rate differs slightly from other trials with the same MRR input variables.

Figure 4.5 shows the increase of MRR with increasing feed rate from level 1 (50 mm/min)

Table 4.5: MRR (mm^3/min) for each trial

Trial number	Feed rate (mm/min)	SS (RPM)	Tool Coating	MRR (mm3/min)
1	50 (L1)	20000 (L1)	no coating (L1)	0.074686
2	50 (L1)	25000 (L2)	HM (L3)	0.074686
3	50 (L1)	30000 (L3)	UT (L2)	0.074686
4	75 (L2)	20000 (L1)	HM (L3)	0.111741
5	75 (L2)	25000 (L2)	UT (L2)	0.111741
6	75 (L2)	30000 (L3)	no coating (L1)	0.112498
7	100 (L3)	20000 (L1)	UT (L2)	0.148604
8	100 (L3)	25000 (L2)	no coating (L1)	0.151073
9	100 (L3)	30000 (L3)	HM (L3)	0.148604

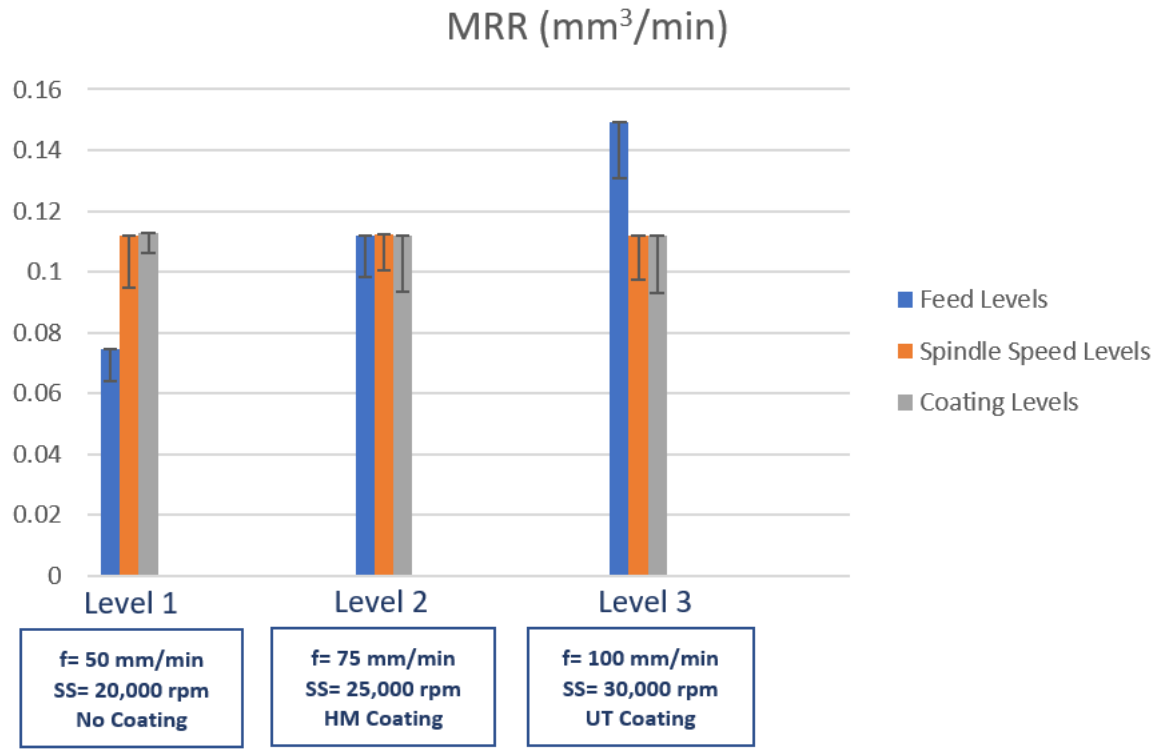

Figure 4.20: Histogram of material removal rate classed according to different levels for each input parameter.

to level 3 (100 mm/min). The coating thickness and spindle speed do not appear to affect the material removal rate greatly.

The effect of the feed rate is translated into the widely used equation to calculate the material removal rate in constant depth milling:

$$MRR(\frac{mm^3}{min}) = a_p a_e f \tag{4.2}$$

where a_p is the depth of cut in mm, a_e is the radial depth of cut in mm and f is the feed rate in mm/min. By definition, the feed rate is the speed of the cutting tool's movement relative to the workpiece as the tool makes the cut. As the feed rate increases, the amount of material removed per tooth increases. That is why the material removal rate increases significantly with increasing feed rate.

4.6 Further Discussion

As feed rate increases, the specific cutting energy decreases thus the process productivity increases. However, there is a trade off between minimising the SCE and minimising the roughness when choosing an optimum feed rate as it is apparent from figure 4.17 that roughness increases with increasing feed rate. In addition, there is a limitation to the feed rate governed by microtools' physical and mechanical capabilities as excessive feed rate would result in tool breakage. For instance, in trial 6 and 8, the failure of the tools before complete machining of the predetermined area could have been caused by the input parameters chosen being out of the capability range for the specific cutting tools used. However, after examining the quality of the tools' cutting edges using SEM imaging, chipping wear was observed and the tools' edges were not sharp. Generally, during the initial "stable" part in machining, the cutting tool is still relatively sharp and its edges are being gradually smoothened thus the pressure on the tool is decreased. After this stage, the tool starts to wear out with increase in cutting forces until it reaches a critical stage where it fails. For the uncoated tools in trials 6 and 8, the relatively stable part of machining was cut short as they have reached a critical wear stage prematurely due to the initial wear they presented before machining. If we take a look at the force values presented in table 4.2, it is evident that the forces in trials 6 and 8 (0.22 N and 0.38 N) are high which shows the effect of tool sharpness and tool coating on tool performance. Although feed rate and spindle speeds contribute to higher forces acting on the tool, a big impact would be attributed to the tool coating and the sharpness of the tool. If we compare trial 6 (uncoated) and 9 (HM), we can see that the feed rate for trial 6 is 75 mm/min lower than feed rate of trial 9 which is 100 mm/min, the spindle speeds are the

same. If the resultant forces were affected by feed rate primarily, one would expect that the resultant force for trial 8 will be higher than that for trial 9. However, the results showed that the resultant force for trial 9 is lower than that for trial 6. This shows that the coating and sharpness of the tool plays the biggest role in determining the resultant cutting force. This is corroborated by literature which implies that worn tools exhibit higher cutting forces than sharp tools which leads to their failure [92]. The presence of BUE on UT coated tools reflected on the roughness of the machined surfaces as predicted in chapter 4.1. The roughness measured on surface of samples from trial 3 and 5 (trials of tools with UT coating and highest BUE amount) are relatively high; 0.2 μm and 0.39 μm respectively. Analysis of variance could not be performed as having two failed trials (6 and 8) renders the method statistically invalid. However, The results give a qualitative indication as to what the optimum levels are among the levels tested. Tool coating has proven to be a very significant factor for the longevity of the tool and the quality of the surface produced.

4.7 Secondary Experiments: Testing DLC coated tools' performance

After completing the initial experimental work according to Taguchi's orthogonal L9 array with HM and UT coated tools, successful DLC coating of 200 μm microns diameter microtools was achieved with two thickness variations; 300 and 400 nm. The performance of these tools in micromilling was tested at low feed (50 mm/min) and low spindle speed (20,000 rpm) with the same milling strategy as the previous experimental trials and benchmarked at the same cutting parameters with an HM coated tool. The table below denotes the secondary experiments (machining trials) and their roughness measurement results.

Secondary experiments	**Coating**	**Ra μm**	**Sharpness Quality (Pre-trial)**
Trial 1	HM	0.102	sharp
Trial 2	DLC, 300 nm	0.105	Not very sharp
Trial 3	DLC, 400 nm	0.315	Severely eroded

From the results and SEM images of the tools pre-trial (figure **??**) we can see that even though the sharpness of DLC coated tools is not nearly as good as the sharpness of the HM coated tool, the performance of the DLC coated tool with 300 nm thickness is closely comparable to the HM coated tool in terms of surface quality produced.

Chapter 5

Conclusions

First, literature review on structured surfaces, end mill coatings, micromilling of titanium alloys and design of experiment has allowed the formulation of a methodology to be followed in order to test a selective variety of machining parameters and tool coatings on machining outputs such as Ra, MRR and SCE. Testing of commercially available tooling through micromilling experiments and in-house development of coatings have been achieved. After performing micromilling experiments and comparing output parameters together as functions of input parameters, it was concluded that tool coating has a very big impact ofquality of machining and tool life while micromachining of Ti-6Al-4V. Although ANOVA could not be applied to determine the optimal combination of parameters and coatings, the performance of the HM coated tool (TiAlN based coating) in terms of machined sample roughness, SCE, MRR and BUE has shown that a 6 μm thick TiAlN/CrAlN coating performed better over a 4 μm thick TiCN/TiAlCrN based coating and either coating performed far better than a pristine uncoated WC tool. Also, the sharpness of uncoated tool played a very big role skewing the experimental array which rendered the application of ANOVA invalid. The titanium alloy with the combination of right machining parameters (low feed rate of 50 mm/min, low spindle speed of 20,000 RPM and the right use of coating type such as TiAlN/CrAlN coating produced an average roughness of 0.1 to 0.15 micron while machined on a KERN Evo Machine The machining performance was found to be relatively repeatable over a large area machined (corresponding to an MRR of about 0.1 mm^3/min and specific cutting energy of about 25 to 30 J/mm^3).Furthermore, a tradeoff lies between minimising Ra, SCE and maximising

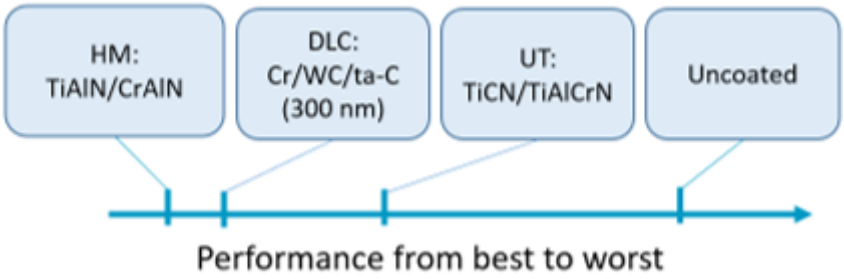

Figure 5.1: Initial classification of tested tool coatings

MRR. Coating material and the feed of the tool seem to be at the heart of this tradeoff since minimising Ra requires low feed and minimising SCE and maximising MRR requires high feed and good coating material. However, tool life should not be neglected either as a feed that is too high increases the risk of tool breakage and increases tool wear rate. Finally, the secondary experimental runs conducted allow an initial classification of the DLC coated tools within the capabilities of the commercial tested tools.Figure 5.1 presents the classification of the tested tool according to the roughness measurements firstly, SCE, MRR and BUE formation.

Chapter 6

Recommendations and Future Work

Although micro endmills were successfully coated with DLC using HiPIMS method and experimentation was done in order to evaluate the performance of these tools coating against tested commercial coatings, time limitations did not allow a systematic design of experiment to be conducted with these tools. It is postulated that the window of DLC deposition provides a wide room to play with tunable properties ((through varied thicknesses, varied sp^3/sp^2 content etc.) and thus, DLC coatings can outlast both TiAlN and TiCN based coatings. Beside the fact that they are harder ($\approx$ 4000 Vickers) than the two aforementioned coatings, their adhesion would be enhanced because of the deposition by HiPIMS technology. Thus, future work includes testing these tools and bench-marking them against the commercially acquired coated tools in a systematic DOE. In addition, procuring sharper uncoated tools and repeating trials 1, 6 and 8 would be very interesting as it would allow, firstly, the validation of the results obtained in this work regarding the effect of tool coating on the longevity of the tool life and, secondly, the application of statistical methods to find the optimum parameters along with coating type for micromilling Ti-6Al-4V in the parameter-space chosen (the three level of DOE). Finally, manufacturing structured surfaces using optimised cutting parameters and coating would be very beneficial as it would allow the exploration of inducing a functionality on Ti-6Al-4V surfaces such as hydrophobicity through micromilling.

References

[1] C. Veiga, J. P. Davim, and A. J. Loureiro, "Review on machinability of titanium alloys: The process perspective," *Reviews on Advanced Materials Science*, vol. 34, no. 2, pp. 148–164, 2013.

[2] C. Liu, S. Goel, I. Llavori, P. Stolf, C. L. Giusca, A. Zabala, J. Kohlscheen, J. M. Paiva, J. L. Endrino, S. C. Veldhuis, and G. S. Fox Rabinovich, "Benchmarking of several material constitutive models for tribology, wear, and other mechanical deformation simulations of Ti6Al4V," *Journal of the Mechanical Behavior of Biomedical Materials*, vol. 97, no. May, pp. 126–137, 2019.

[3] C. Veiga, J. P. Davim, and A. Loureiro, "Properties and applications of titanium alloys : A brief review PROPERTIES AND APPLICATIONS OF TITANIUM ALLOYS : A BRIEF REVIEW," no. July 2016, 2012.

[4] S. Zhang, Y. Zhou, H. Zhang, Z. Xiong, and S. To, "Advances in ultra-precision machining of micro-structured functional surfaces and their typical applications," *International Journal of Machine Tools and Manufacture*, vol. 142, no. May, pp. 16–41, 2019.

[5] L. Wang, "Use of structured surfaces for friction and wear control on bearing surfaces," *Surface Topography: Metrology and Properties*, vol. 2, no. 4, 2014.

[6] C. G. Jothi Prakash and R. Prasanth, "Enhanced boiling heat transfer by nano structured surfaces and nanofluids," *Renewable and Sustainable Energy Reviews*, vol. 82, no. August 2016, pp. 4028–4043, 2018.

[7] J. Yu, S. W. Kang, T. S. Kwon, and D. Banerjee, "In situ characterization of enhanced thermal performance by periodic nanostructures on the surface of a mi-

crochannel," *International Journal of Heat and Mass Transfer*, vol. 124, pp. 414–422, 2018.

[8] Y. Lin, H. Chen, G. Wang, and A. Liu, "Recent Progress in Preparation and Anti-Icing Applications of Superhydrophobic Coatings," *Coatings*, vol. 8, no. 6, p. 208, 2018.

[9] M. Ribeiro, F. J. Monteiro, and M. P. Ferraz, "Infection of orthopedic implants with emphasis on bacterial adhesion process and techniques used in studying bacterial-material interactions," *BioMatter*, vol. 2, no. 4, pp. 176–194, 2012.

[10] C. Aboltins, J. Daffy, P. Choong, and P. Stanley, "Current concepts in the management of prosthetic joint infection Microbiology of PJI," vol. 44, 2014.

[11] C. Yue, C. Yue, B. Zhao, Y. Ren, R. Kuijer, H. C. V. D. Mei, H. J. Busscher, and E. T. J. Rochford, "THE IMPLANT INFECTION PARADOX : WHY DO SOME SUCCEED WHEN OTHERS FAIL ? OPINION AND DISCUSSION PAPER," vol. 29, pp. 303–313, 2015.

[12] A. Shokrani, V. Dhokia, and S. T. Newman, "Comparative investigation on using cryogenic machining in CNC milling of Ti-6Al-4V titanium alloy," *Machining Science and Technology*, vol. 20, no. 3, pp. 475–494, 2016.

[13] R. M. Saoubi, S. T. Ab, J. C. Outeiro, H. Chandrasekaran, O. W. D. Jr, and I. S. Jawahir, "A review of surface integrity in machining and its impact on functional performance and life of machined products," vol. 1, pp. 203–236, 2008.

[14] D. Ulutan and T. Ozel, "Machining induced surface integrity in titanium and nickel alloys : A review," *International Journal of Machine Tools and Manufacture*, vol. 51, no. 3, pp. 250–280, 2011.

[15] R. Phenomena, E. S. P. B. V, and B. R. Chakraborty, "STUDY OF THE CHEMICAL BONDING OF TITANIUM WITH SILICON AND OXYGEN BY AES AND SEELS," vol. 50, pp. 185–194, 1990.

[16] G. C. Requena, *Phase transformation kinetics during continuous heating of $\alpha + \beta$ and β metastable titanium alloys*. PhD thesis, 2015.

[17] R. J. Lancashire, "Lecture 5a. Structure of the elements (Groups 1 and 2 metals)," 2014.

[18] H. Xu, D. Ye, and L. Mei, "A study of the back stress and the friction stress behaviors of Ti-6Al-4V alloy during low cycle fatigue at room temperature Materials Science & Engineering A A study of the back stress and the friction stress behaviors of Ti-6Al-4V alloy during low cycle," *Materials Science & Engineering A*, vol. 700, no. June, pp. 530–539, 2017.

[19] A. K. Geim, S. V. Dubonos, I. V. Grigorieva, K. S. Novoselov, A. A. Zhukov, and S. Y. Shapoval, "Microfabricated adhesive mimicking gecko foot-hair," *Nature Materials*, vol. 2, no. 7, pp. 461–463, 2003.

[20] L. Ge, S. Sethi, L. Ci, P. M. Ajayan, and A. Dhinojwala, "Carbon nanotube-based synthetic gecko tapes," *Proceedings of the National Academy of Sciences*, vol. 104, no. 26, pp. 10792–10795, 2007.

[21] Q. Li, "A practical fabrication method of the gecko-inspired easy-removal skin adhesives," *Biosurface and Biotribology*, vol. 3, no. 2, pp. 66–74, 2017.

[22] S. S. Latthe, C. Terashima, K. Nakata, and A. Fujishima, "Superhydrophobic surfaces developed by mimicking hierarchical surface morphology of lotus leaf," *Molecules*, vol. 19, no. 4, pp. 4256–4283, 2014.

[23] H. X. Huang and X. Wang, "Biomimetic fabrication of micro-/nanostructure on polypropylene surfaces with high dynamic superhydrophobic stability," *Materials Today Communications*, vol. 19, no. April, pp. 487–494, 2019.

[24] T. C. Hobaek, K. G. Leinan, H. P. Leinaas, and C. Thaulow, "Surface Nanoengineering Inspired by Evolution," *BioNanoScience*, vol. 1, no. 3, pp. 63–77, 2011.

[25] M. Fimberger, A. Behrendt, G. Jakopic, F. Stelzer, V. Kumbaraci, and F. Wiesbrock, "Modification Pathways for Copoly (2-oxazoline) s Enabling Their Application as Antireflective Coatings in Photolithography," *Macromolecular Rapid Communications*, vol. 37, no. 3, pp. 233–238, 2016.

[26] J. K. Kim, S. Chhajed, M. F. Schubert, E. F. Schubert, A. J. Fischer, M. H. Crawford, J. Cho, H. Kim, and C. Sone, "Light-extraction enhancement of GaInN light-emitting diodes by graded-refractive-index indium tin oxide anti-reflection contact," *Advanced Materials*, vol. 20, no. 4, pp. 801–804, 2008.

[27] C. M. Ruiz, C. Algora, O. Vigil, D. Martin, V. Bermudez, and E. Dieguez, "Transparent Conducting Oxides As Antireflection Coatings for GaSb TPV Cells," no. January, pp. 221–229, 2004.

[28] W. Li, X. Tan, J. Zhu, P. Xiang, T. Xiao, L. Tian, A. Yang, M. Wang, and X. Chen, "Broadband antireflective and superhydrophobic coatings for solar cells," *Materials Today Energy*, vol. 12, pp. 348–355, 2019.

[29] M. Burghoorn, D. Roosen-Melsen, J. de Riet, S. Sabik, Z. Vroon, I. Yakimets, and P. Buskens, "Single layer broadband anti-reflective coatings for plastic substrates produced by full wafer and roll-to-roll step-and-flash nano-imprint lithography," *Materials*, vol. 6, no. 9, pp. 3710–3726, 2013.

[30] H. T. Wang, W. B. Lee, J. Chan, and S. To, "Numerical and experimental analysis of heat transfer in turbulent flow channels with two-dimensional ribs," *Applied Thermal Engineering*, vol. 75, pp. 623–634, 2015.

[31] Y. F. Missirlis, M. Katsikogianni, and Y. F. Missirlis, "CONCISE REVIEW OF MECHANISMS OF BACTERIAL ADHESION TO BIOMATERIALS AND OF TECHNIQUES USED IN ESTIMATING BACTERIA- MATERIAL INTERACTIONS," *European cells and materials*, vol. 8, pp. 37–57, 2004.

[32] J. Hasan, R. J. Crawford, and E. P. Ivanova, "Antibacterial surfaces: The quest for a new generation of biomaterials," *Trends in Biotechnology*, vol. 31, no. 5, pp. 295–304, 2013.

[33] C. M. Magin, S. P. Cooper, and A. B. Brennan, "Non-toxic antifouling strategies," *Materials Today*, vol. 13, no. 4, pp. 36–44, 2010.

[34] A. W. Feinberg, J. F. Schumacher, and A. B. Brennan, "Engineering high-density endothelial cell monolayers on soft substrates," *Acta Biomaterialia*, vol. 5, no. 6, pp. 2013–2024, 2009.

[35] A. C. Seward, "A Contribution to our Knowledge of Wealden Floras, with especial reference to a Collection of Plants from Sussex," *Quarterly Journal of the Geological Society*, vol. 69, no. 1-4, pp. 85–116, 2009.

[36] C. D. Bandara, S. Singh, I. O. Afara, A. Wolff, T. Tesfamichael, K. Ostrikov, and A. Oloyede, "Bactericidal Effects of Natural Nanotopography of Dragonfly Wing on Escherichia coli," *ACS Applied Materials and Interfaces*, vol. 9, no. 8, pp. 6746–6760, 2017.

[37] G. S. Watson, D. W. Green, L. Schwarzkopf, X. Li, B. W. Cribb, S. Myhra, and J. A. Watson, "A gecko skin micro/nano structure - A low adhesion, superhydrophobic, anti-wetting, self-cleaning, biocompatible, antibacterial surface," *Acta Biomaterialia*, vol. 21, pp. 109–122, 2015.

[38] X. Li and T. Chen, "Enhancement and suppression effects of a nanopatterned surface on bacterial adhesion," vol. 052419, pp. 1–7, 2016.

[39] E. P. Ivanova, J. Hasan, H. K. Webb, G. Gervinskas, S. Juodkazis, V. K. Truong, A. H. F. Wu, R. N. Lamb, V. A. Baulin, G. S. Watson, J. A. Watson, D. E. Mainwaring, and R. J. Crawford, "Bactericidal activity of black silicon," *Nature Communications*, pp. 1–7, 2013.

[40] P. W. May, M. Clegg, T. A. Silva, H. Zanin, O. Fatibello-Filho, V. Celorrio, D. J. Fermin, C. C. Welch, G. Hazell, L. Fisher, A. Nobbs, and B. Su, "Diamond-coated 'black silicon' as a promising material for high-surface-area electrochemical electrodes and antibacterial surfaces," *Journal of Materials Chemistry B*, vol. 4, no. 34, pp. 5737–5746, 2016.

[41] T. Sjöström, A. H. Nobbs, and B. Su, "Bactericidal nanospike surfaces via thermal oxidation of Ti alloy substrates," *Materials Letters*, vol. 167, pp. 22–26, 2016.

[42] D. W. Green, K. K. H. Lee, J. A. Watson, H. Y. Kim, K. S. Yoon, E. J. Kim, J. M. Lee, G. S. Watson, and H. S. Jung, "High Quality Bioreplication of Intricate Nanostructures from a Fragile Gecko Skin Surface with Bactericidal Properties," *Scientific Reports*, vol. 7, no. June 2016, pp. 1–12, 2017.

[43] M. N. Dickson, E. I. Liang, L. A. Rodriguez, N. Vollereaux, and A. F. Yee, "Nanopatterned polymer surfaces with bactericidal properties," *Biointerphases*, vol. 10, no. 2, p. 021010, 2015.

[44] L. E. Fisher, Y. Yang, A. Hobbs, M.-F. Yuen, W. Zhang, and B. Su, "Bactericidal activity of biomimetic diamond nanocone surfaces," *Journal of Biomaterials and Biological Interfaces*, 2016.

[45] D. Carou, E. M. Rubio, J. Herrera, C. H. Lauro, J. P. Davim, D. Carou, E. M. Rubio, J. Herrera, C. H. Lauro, and J. P. Davim, "Latest advances in the micro-milling of titanium alloys : a review," *Procedia Manufacturing*, vol. 13, pp. 275–282, 2017.

[46] M. L. Culpepper, T. J. Hodgson, T. R. Kurfess, and R. E. D. Advisor, "International assessment of research and development in micromanufacturing," tech. rep., World Technology Evaluation Center (WTEC), Inc., 2005.

[47] E. Brinksmeier and W. Preuss, "Micro-machining," *Philosophical Transactions of the Royal Society A: Mathematical, Physical and Engineering Sciences*, vol. 370, no. 1973, pp. 3973–3992, 2012.

[48] P. Piljek, Z. Keran, and M. Math, "Micromachining - Review of Literature From 1980 to 2010," *Interdisciplinary Description of Complex Systems*, vol. 12, no. 1, pp. 1–27, 2014.

[49] P. Cardoso and J. P. Davim, "MICRO MILLING OF METALLIC MATERIALS - A BRIEF OVERVIEW," vol. 2, pp. 79–85, 2012.

[50] Y. Li, W. Zhao, S. Lan, J. Ni, W. Wu, and B. Lu, "A review on spindle thermal error compensation in machine tools," *International Journal of Machine Tools and Manufacture*, vol. 95, no. February 2018, pp. 20–38, 2015.

[51] A. Pramanik, "Problems and solutions in machining of titanium alloys," *International Journal of Advanced Manufacturing Technology*, vol. 70, no. 5-8, pp. 919–928, 2014.

[52] A. Dickins, "Fabrication of micro-scale features on titanium alloys through micromilling," 2017.

[53] M. Ziberov, M. B. da Silva, M. Jackson, and W. N. Hung, "Effect of Cutting Fluid on Micromilling of Ti-6Al-4V Titanium Alloy," *Procedia Manufacturing*, vol. 5, no. 2003, pp. 332–347, 2016.

[54] S. N. B. Oliaei and Y. Karpat, "Investigating the influence of built-up edge on forces and surface roughness in micro scale orthogonal machining of titanium alloy Ti6Al4V," *Journal of Materials Processing Technology*, vol. 235, pp. 28–40, 2016.

[55] V. P. Tabakov, A. S. Vereschaka, and A. A. Vereschaka, "Multilayer composition coatings for cutting tools: formation and performance properties," *Mechanics & Industry*, vol. 18, no. 7, p. 706, 2017.

[56] L. L. Alhadeff, M. B. Marshall, D. T. Curtis, and T. Slatter, "Protocol for tool wear measurement in micro-milling," *Wear*, vol. 420-421, no. August 2018, pp. 54–67, 2019.

[57] P. C. Siow, J. A. Ghani, M. J. Ghazali, T. R. Jaafar, M. A. Selamat, and C. H. Che Haron, "Characterization of TiCN and TiCN/ZrN coatings for cutting tool application," *Ceramics International*, vol. 39, no. 2, pp. 1293–1298, 2013.

[58] A. Rizzo, L. Mirenghi, M. Massaro, U. Galietti, L. Capodieci, R. Terzi, L. Tapfer, and D. Valerini, "Improved properties of TiAlN coatings through the multilayer structure," *Surface and Coatings Technology*, vol. 235, pp. 475–483, 2013.

[59] L. Ning, S. C. Veldhuis, and K. Yamamoto, "Investigation of wear behavior and chip formation for cutting tools with nano-multilayered TiAlCrN/NbN PVD coating," *International Journal of Machine Tools and Manufacture*, vol. 48, no. 6, pp. 656–665, 2008.

[60] A. Aramcharoen and P. Mativenga, "The Effect of AlCrTiN Coatings on Product Quality in Micro-milling of 45 HRC Hardened H13 Die Steel," *Proceedings of the 35th International MATADOR Conference*, no. September 2018, pp. 0–4, 2007.

[61] A. Aramcharoen, P. T. Mativenga, S. Yang, K. E. Cooke, and D. G. Teer, "Evaluation and selection of hard coatings for micro milling of hardened tool steel," *International Journal of Machine Tools and Manufacture*, vol. 48, no. 14, pp. 1578–1584, 2008.

[62] W. Darmawan, H. Usuki, I. S. Rahayu, C. Gottlöber, and R. Marchal, "Wear Characteristics of Multilayer-Coated Cutting Tools when Milling Particleboard," *Forest Products Journal*, vol. 60, no. 7, pp. 615–621, 2013.

[63] J. Robertson, "Diamond-like amorphous carbon," vol. 37, pp. 129–281, 2002.

[64] J. Wang, Y. Sugimura, A. Evans, and W. Tredway, "The mechanical performance of DLC films on steel substrates," *Thin Solid Films*, vol. 325, no. 1-2, pp. 163–174, 1998.

[65] PVT Vacuum, "xPro4C," tech. rep.

[66] T. Wu and K. Cheng, "Micro milling performance assessment of diamond-like carbon coatings on a micro-end mill," *Proceedings of the Institution of Mechanical Engineers, Part J: Journal of Engineering Tribology*, vol. 227, no. 9, pp. 1038–1046, 2013.

[67] Z. Liang, P. Gao, X. Wang, S. Li, T. Zhou, and J. Xiang, "Cutting performance of different coated micro end mills in machining of Ti-6Al-4V," *Micromachines*, vol. 9, no. 11, 2018.

[68] Hannibal Carbide Tools, "Titanium coatings for improved performance of wet or dry machining."

[69] E. Santecchia, A. M. Hamouda, F. Musharavati, E. Zalnezhad, M. Cabibbo, and S. Spigarelli, "Wear resistance investigation of titanium nitride-based coatings," *Ceramics International*, vol. 41, no. 9, pp. 10349–10379, 2015.

[70] D. Depla, S. Mahieu, and J. Greene, "Chapter 5 - sputter deposition processes," in *Handbook of Deposition Technologies for Films and Coatings (Third Edition)* (P. M. Martin, ed.), pp. 253 – 296, Boston: William Andrew Publishing, third edition ed., 2010.

[71] J. A. Santiago, I. Fernández-Martínez, A. Wennberg, J. M. Molina-Aldareguia, M. Castillo-Rodríguez, T. C. Rojas, J. C. Sánchez-López, M. U. González, J. M. García-Martín, H. Li, V. Bellido-González, M. A. Monclús, and R. González-Arrabal, "Adhesion enhancement of DLC hard coatings by HiPIMS metal ion etching pretreatment," *Surface and Coatings Technology*, vol. 349, no. May, pp. 787–796, 2018.

[72] J. Antony, S. Warwood, K. Fernandes, H. Rowlands, and J. Antony, "Work Study Emerald Article : Process optimisation using Taguchi methods of experimental design Process optimisation using Taguchi methods of experimental design," 2007.

[73] V. C. Zitrom, "One-Factor-at-a-Time Versus Designed Experiments," 1999.

[74] G. Taguchi, W. W. Ii, G. Taguchi, R. Design, and R. Design, "TAGUCHI ' S METHODOLOGY," pp. 73–89.

[75] S. Kamaruddin, Z. A. Khan, and S. H. Foong, "Application of Taguchi Method in the Optimization of Injection Moulding Parameters for Manufacturing Products from Plastic Blend," vol. 2, no. 6, 2010.

[76] K. Suresh, "An overview of randomization techniques: An unbiased assessment of outcome in clinical research," *Journal of Human Reproductive Sciences*, vol. 4, no. 1, pp. 8–11, 2011.

[77] W. B. Rashid, S. Goel, J. P. Davim, and S. N. Joshi, "Parametric design optimization of hard turning of AISI 4340 steel (69 HRC)," *International Journal of Advanced Manufacturing Technology*, vol. 82, no. 1-4, pp. 451–462, 2016.

[78] R. McFatter, "Computational Formulas for ANOVA," tech. rep., 2013.

[79] P. K. Chu and L. Li, "Characterization of amorphous and nanocrystalline carbon films," *Materials Chemistry and Physics*, vol. 96, no. 2-3, pp. 253–277, 2006.

[80] A. David, K. Lee, and D. A. Dornfeld, "Consortium on Deburring and Edge Finishing A STUDY OF SURFACE ROUGHNESS IN THE MICRO-END-MILLING," 2004.

[81] R. Wang, B. Wang, G. C. Barber, J. Gu, and J. David Schall, "Models for prediction of surface roughness in a face milling process using triangular inserts," *Lubricants*, vol. 7, no. 1, 2019.

[82] E. P. Ivanova, V. K. Truong, H. K. Webb, V. A. Baulin, J. Y. Wang, N. Mohammodi, F. Wang, C. Fluke, and R. J. Crawford, "Differential attraction and repulsion of Staphylococcus aureus and Pseudomonas aeruginosa on molecularly smooth titanium films," *Scientific Reports*, vol. 1, pp. 1–8, 2011.

[83] D. E. Newbury, "Mistakes encountered during automatic peak identification of minor and trace constituents in electron-excited energy dispersive X-ray microanalysis," *Scanning*, vol. 31, no. 3, pp. 91–101, 2009.

[84] M. Wang and S. Miyake, "Surface Morphology and Tribological Properties of Nanoscale (Ti, Al, Si, C)N Multilayer Coatings Deposited by Reactive Magnetron Sputtering," in *Lubrication - Tribology, Lubricants and Additives*, pp. 77–100, 2018.

[85] A. A. Vereschaka, S. N. Grigoriev, N. N. Sitnikov, G. V. Oganyan, and A. Batako, "Surface & Coatings Technology Working e ffi ciency of cutting tools with multilayer nano-structured Ti-TiCN- (Ti , Al) CN and Ti-TiCN- (Ti , Al , Cr) CN coatings : Analysis of cutting properties , wear mechanism and di ff usion processes," vol. 332, no. October, pp. 198–213, 2017.

[86] C.-m. Kao, J.-w. Lee, H.-w. Chen, Y.-c. Chan, J.-g. Duh, and S.-p. Chen, "Microstructures and mechanical properties evaluation of TiAlN / CrSiN multilayered thin fi lms with different bilayer periods," *Surface & Coatings Technology*, vol. 205, no. 5, pp. 1438–1443, 2010.

[87] I. Ucun, K. Aslantasx, B. Gökcxe, and F. Bedir, "Effect of tool coating materials on surface roughness in micromachining of Inconel 718 super alloy," *Proceedings of the*

Institution of Mechanical Engineers, Part B: Journal of Engineering Manufacture, vol. 228, no. 12, pp. 1550–1562, 2014.

[88] Z. Wang, V. Kovvuri, A. Araujo, M. Bacci, W. N. Hung, and S. T. Bukkapatnam, "Built-up-edge effects on surface deterioration in micromilling processes," *Journal of Manufacturing Processes*, vol. 24, pp. 321–327, 2016.

[89] E. Abele, B.-a. Behrens, D. Biermann, and B. Denkena, "Measurement and Test Techniques," no. January 2015, 2013.

[90] Electronics Tutorials, "Butterworth Filter Design."

[91] A. Sainath and G. L. Samuel, "Modelling and verification of stability of micro-milling process," *International Journal of Machining and Machinability of Materials*, vol. 16, no. 3-4, pp. 229–258, 2014.

[92] X. Chuangwen, D. Jianming, C. Yuzhen, L. Huaiyuan, S. Zhicheng, and X. Jing, "The relationships between cutting parameters, tool wear, cutting force and vibration," *Advances in Mechanical Engineering*, vol. 10, no. 1, pp. 1–14, 2018.

Appendix

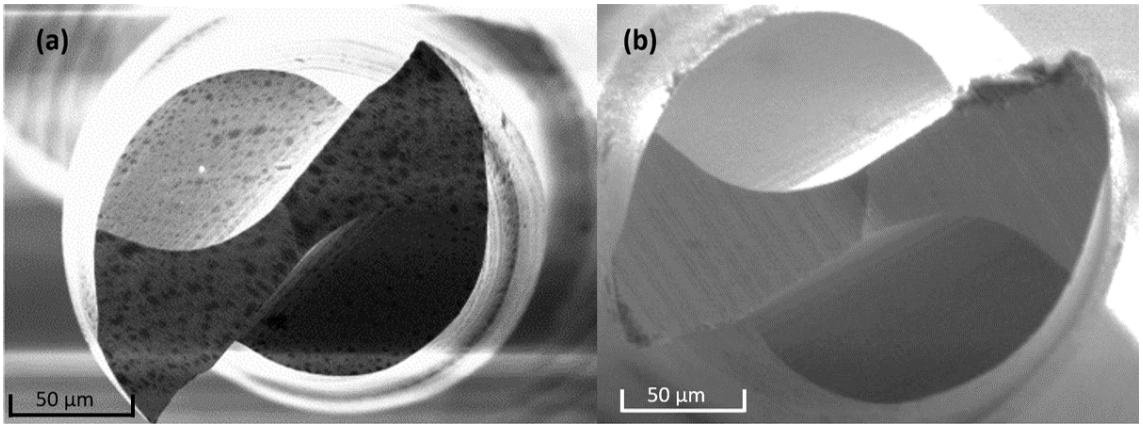

Figure 6.1: SEM image of tool 1 (a) before (b) after machining.

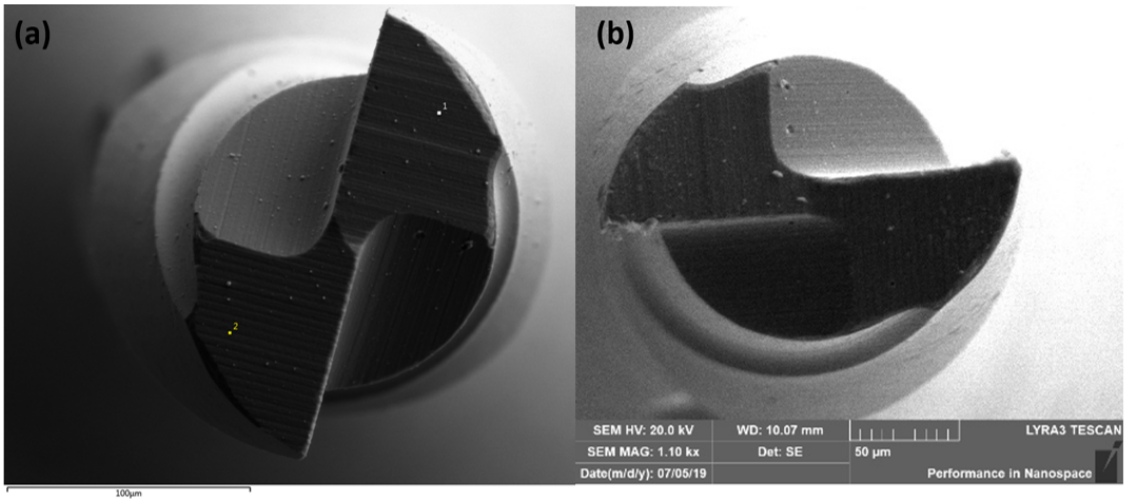

Figure 6.2: SEM image of HLS 1 (a) before (b) after machining.

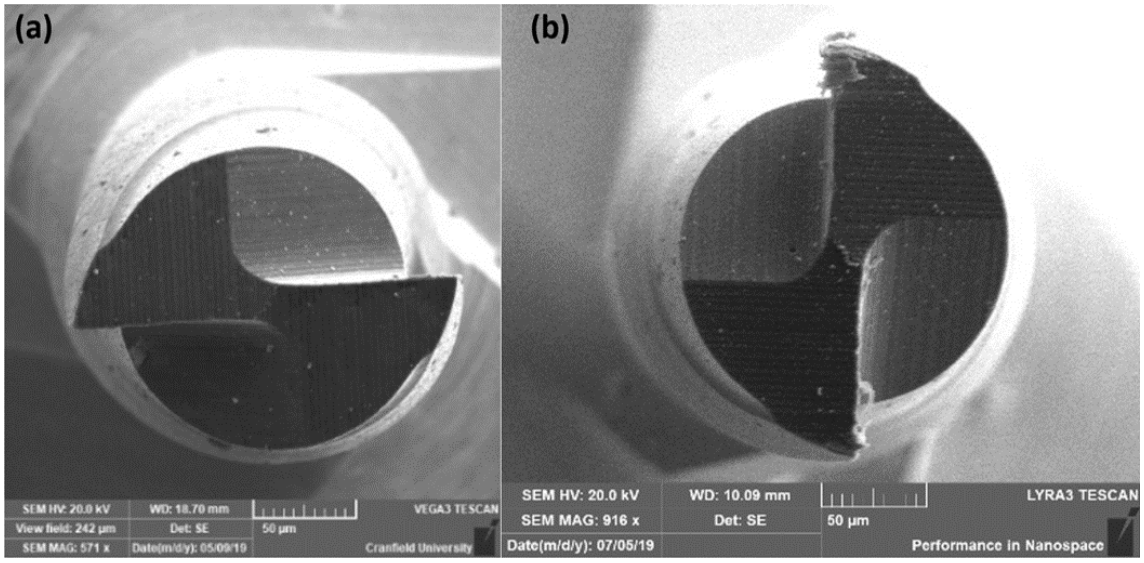

Figure 6.3: SEM image of CES 1 (a) before (b) after machining.

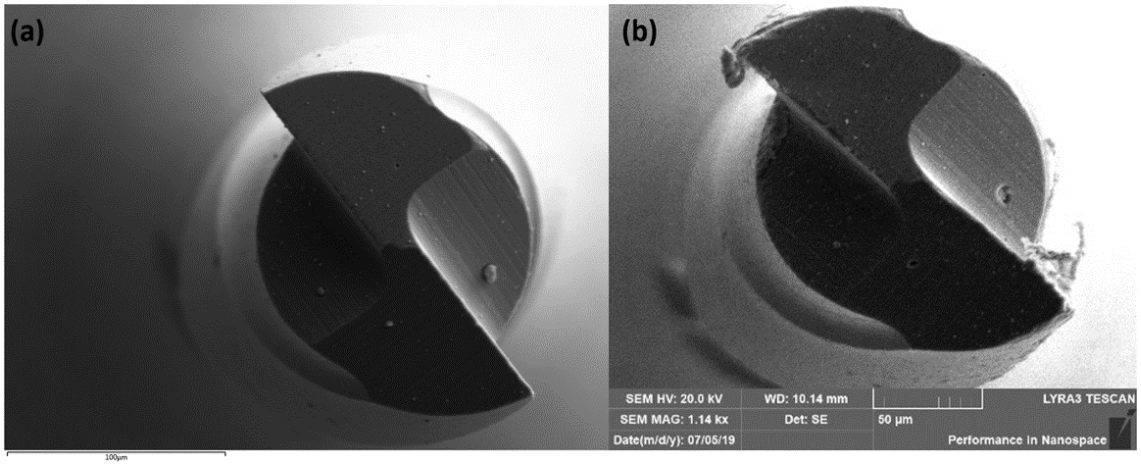

Figure 6.4: SEM image of tool 1 (a) before (b) after machining.

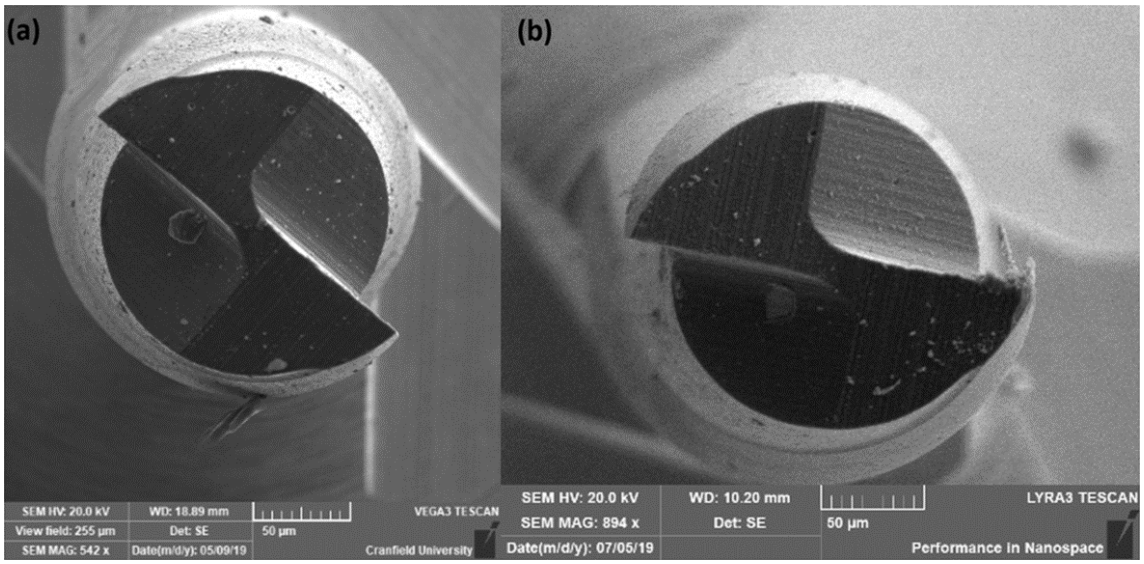

Figure 6.5: SEM image of HLS 1 (a) before (b) after machining.

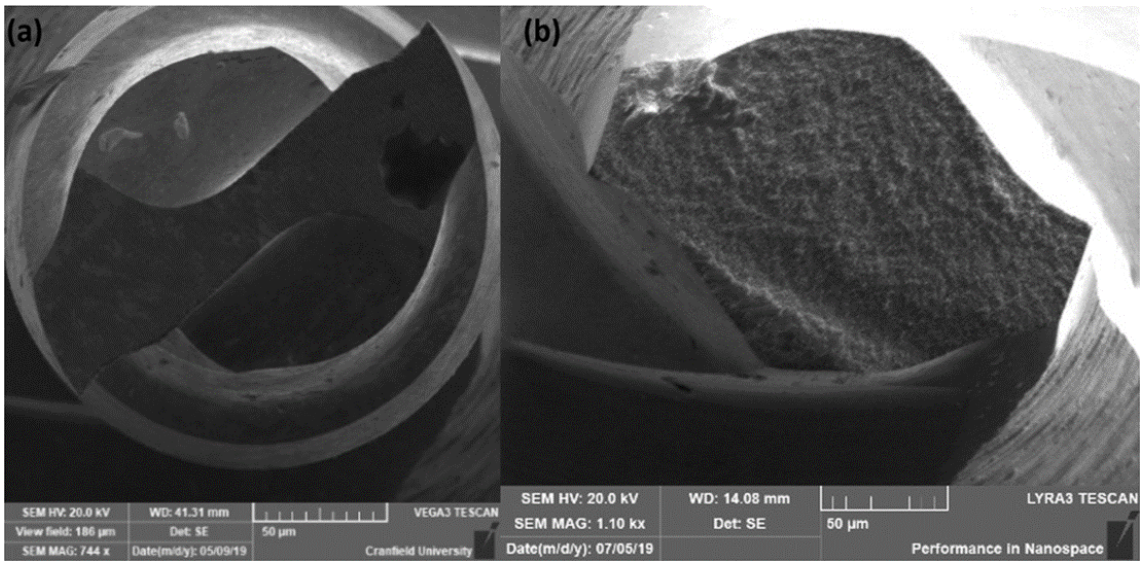

Figure 6.6: SEM image of CES 1 (a) before (b) after machining.

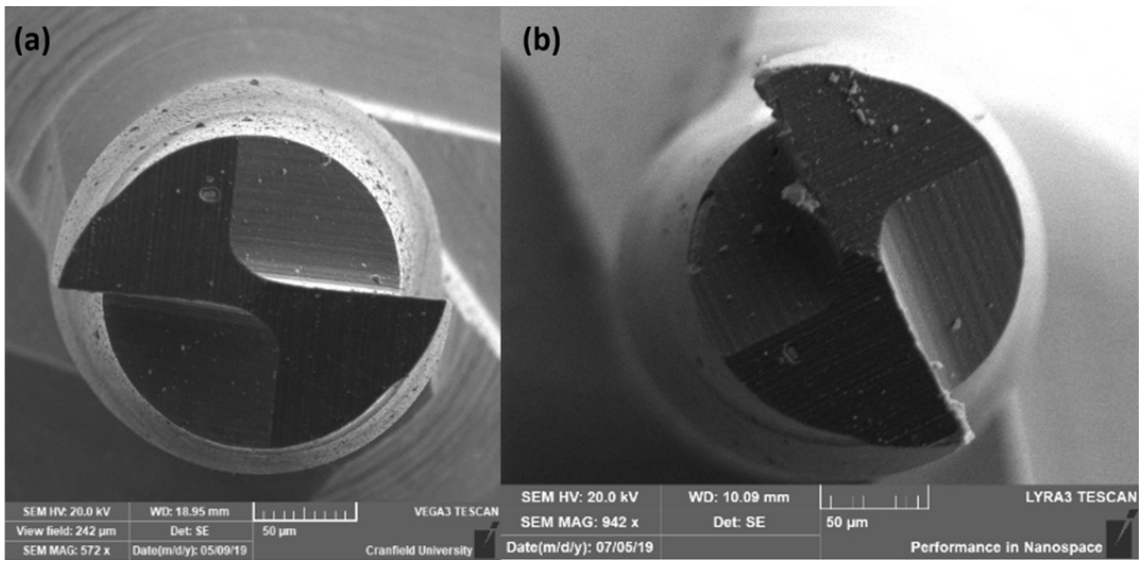

Figure 6.7: SEM image of tool 1 (a) before (b) after machining.

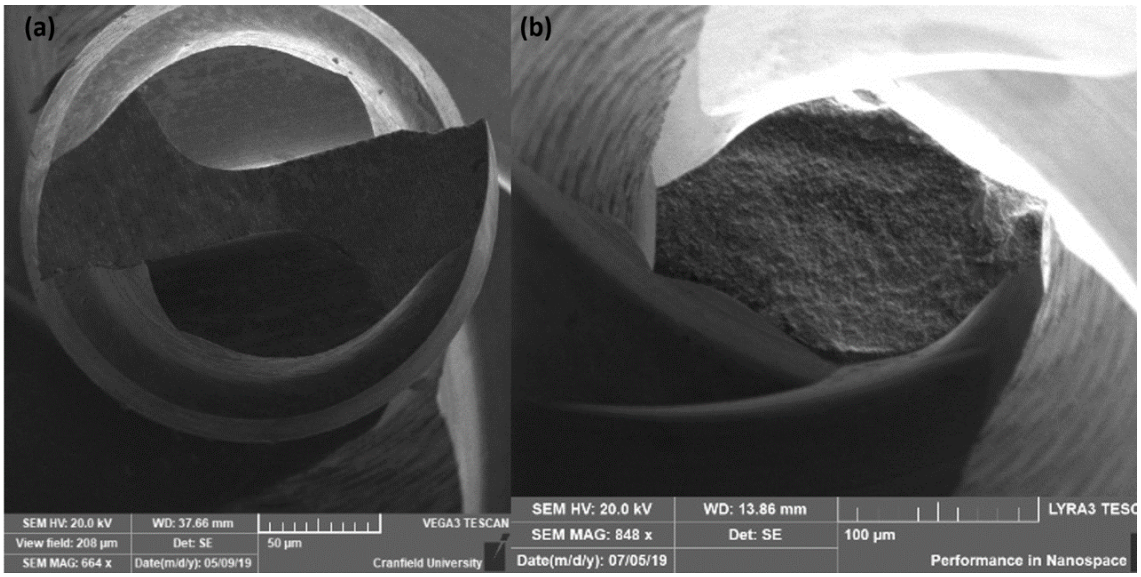

Figure 6.8: SEM image of HLS 1 (a) before (b) after machining.

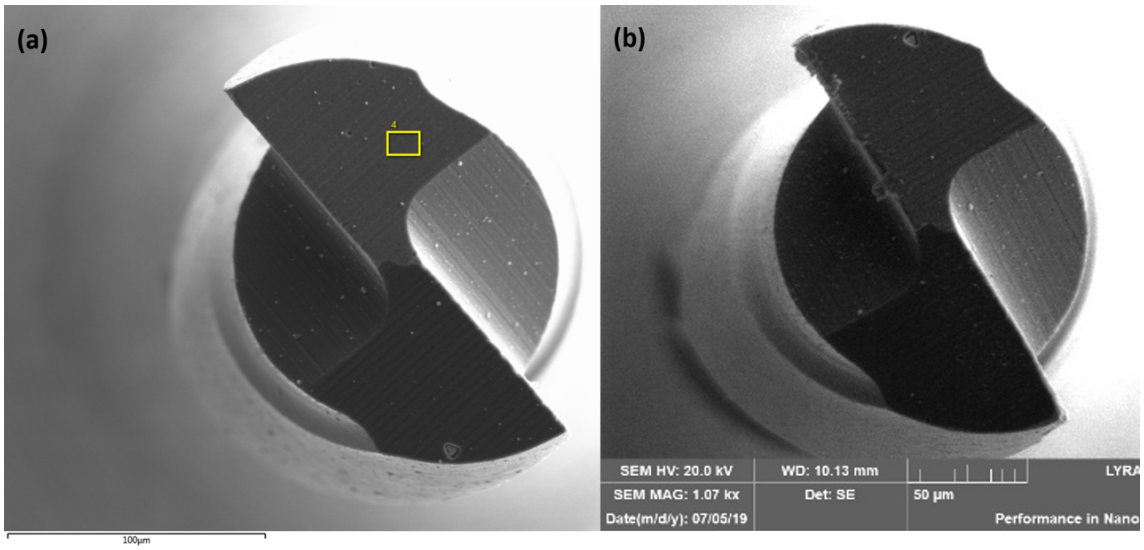

Figure 6.9: SEM image of CES 1 (a) before (b) after machining.